



**HAL**  
open science

# Cold molecules in HI 21 cm absorbers across redshifts $\sim 0.1-4$

F. Combes, N. Gupta

► **To cite this version:**

F. Combes, N. Gupta. Cold molecules in HI 21 cm absorbers across redshifts  $\sim 0.1-4$ . *Astronomy and Astrophysics - A&A*, 2024, 683, pp.A20. 10.1051/0004-6361/202348386 . hal-04484763

**HAL Id: hal-04484763**

**<https://hal.science/hal-04484763>**

Submitted on 29 Feb 2024

**HAL** is a multi-disciplinary open access archive for the deposit and dissemination of scientific research documents, whether they are published or not. The documents may come from teaching and research institutions in France or abroad, or from public or private research centers.

L'archive ouverte pluridisciplinaire **HAL**, est destinée au dépôt et à la diffusion de documents scientifiques de niveau recherche, publiés ou non, émanant des établissements d'enseignement et de recherche français ou étrangers, des laboratoires publics ou privés.

# Cold molecules in H I 21 cm absorbers across redshifts $\sim 0.1$ – $4$ \*

F. Combes<sup>1</sup>  and N. Gupta<sup>2</sup> 

<sup>1</sup> Observatoire de Paris, LERMA, Collège de France, CNRS, PSL University, Sorbonne University, 75014 Paris, France  
e-mail: francoise.combes@obspm.fr

<sup>2</sup> Inter-University Centre for Astronomy and Astrophysics, Post Bag 4, Ganeshkhind, Pune 411 007, India

Received 25 October 2023 / Accepted 6 December 2023

## ABSTRACT

Absorption lines at high-redshift in front of quasars are quite rare in the millimeter (mm) domain. Only five associated and five intervening systems have been reported in the literature. Nevertheless, these discoveries provide very useful information that is complementary to emission lines, allowing, for instance, to distinguish between inflows and outflows. These lines are also good candidates for studying the variations of the fundamental constants of physics. Here we report the findings of our search for CO and other molecules in emission and absorption in front of a sample of 30 targets, comprising 16 associated and 14 intervening H I 21 cm absorbers. The observations were made with the IRAM-30 m telescope simultaneously at 3 mm and 2 mm, exploring several lines of the CO ladder and HCO<sup>+</sup>, depending on the redshift. We detected eight targets in emission, of which five are new. The derived molecular gas masses range from  $10^9$  to  $7 \times 10^{11} M_{\odot}$  and the highest redshift detection ( $z = 3.387$ ) corresponds to a relatively average-metallicity damped Lyman- $\alpha$  absorber for this redshift. We also report four new detections in absorption. Two of the associated CO absorption line detections at high-redshift ( $z = 1.211$  and  $1.275$ ) result from high-spatial-resolution follow-up observations with NOEMA. The disparity between the mm molecular and H I 21 cm absorption lines for these and another intervening system detected in HNC at  $z = 1.275$  is attributable to radio and mm sight lines tracing different media. We compare the atomic and molecular column densities of 14 known high-redshift ( $z > 0.1$ ) molecular absorption line systems. The associated H I absorption lines are broad and exhibit multiple components, and the molecular absorption generally corresponds to the broader and weaker 21 cm absorption component. This indicates two distinct phases: one near galaxy centers with a larger CO-to-H I abundance ratio, and another with lower molecular abundance in the outer regions of the galaxy. In comparison, intervening absorption profiles correspond primarily to H I-dominated gas structure in galaxy outskirts, except for gas at low impact parameters in gravitationally lensed systems. The comparison of interferometric and single-dish observations presented here shows that the detection of absorption requires sufficient spatial resolution to overcome the dilution by emission and will be an important criterion for mm follow-up of 21 cm absorbers from ongoing large-scale surveys.

**Key words.** galaxies: ISM – quasars: absorption lines – quasars: individual: PKS 0201+113 – quasars: individual: PKS 1200+045 – quasars: individual: PKS 1245-19 – quasars: individual: PKS 1406-076

## 1. Introduction

The star formation history of the Universe is characterized by a peak about 10 billion years ago. The star formation rate (SFR) density in galaxies, as reviewed by Madau & Dickinson (2014), evolves across cosmic time: it first increases with time ( $z > 2$ ), peaks at  $z \sim 1$ – $2$ , and then decreases by an order of magnitude from  $z \sim 1$  to the present day. Two main factors are suspected to produce this evolution: the gas content of galaxies, and their star formation efficiency (SFE). From studies of main sequence star-forming galaxies across the Hubble time, the gas fraction in the interstellar medium (ISM) of galaxies appears to be the dominant factor in comparison to the SFE (e.g., Tacconi et al. 2018). It is therefore crucial to constrain the molecular gas content of galaxies over cosmic time, and also its precursor, that is, the atomic gas reservoir. Obreschkow & Rawlings (2009a,b) used theoretical models and the knowledge of molecular gas content of high-redshift galaxies to make very useful predictions of the cosmic evolution of H I and H<sub>2</sub> gas components. The H I evolution was found to be relatively constant over  $z = 1$ – $5$  from damped Lyman- $\alpha$  absorber (DLA) studies, while the H<sub>2</sub>/H I ratio was steeply declining with time, as  $(1+z)^{1.6}$ . Since then, many

molecular line surveys have refined our knowledge, and shown that the cosmic H<sub>2</sub> evolution might be flatter (Decarli et al. 2020; Riechers et al. 2020; Lenkić et al. 2020). In this context, it is important to pursue blind surveys, such as serendipitous discoveries of CO lines in the field of view of the Atacama Large Millimeter/submillimeter Array (ALMA) calibration sources (e.g., Hmanowicz et al. 2023), to obtain an unbiased view of the gas evolution.

Our knowledge of molecular gas in galaxies at high-redshift has received major boosts since the first discovery by Solomon et al. (1992), first by gravitational lensing, as reviewed by Solomon & Vanden Bout (2005), and then through the negative  $K$ -correction thanks to which the CO molecule can be observed over the entirety of its rotation ladder, with the flux density increasing strongly with the  $J$ -level (e.g., Combes et al. 1999). Although more difficult to detect, molecular absorption lines can bring new and complementary information. While the strength of emission lines decreases as a steep function of redshift, absorption lines can be observed as easily at high-redshift as in the local Universe provided there exists a strong background radio source (e.g., Combes 2008). Further, while emission lines are sensitive to dense and warm molecular gas, absorption lines arise in the low-excitation and diffuse gas (e.g., Wiklind & Combes 1994, 1996b, 1997; Menten et al. 2008; Henkel et al. 2009; Muller et al. 2014; Wiklind et al. 2018). In

\* Based on observations carried out with the IRAM-30 m telescope and NOEMA, the Northern Extended Millimeter Array – IRAM (Institute of Radioastronomy in Millimeter).

conclusion, with a 3 mm continuum source flux density of at least  $\sim 50$  mJy, absorption lines can be potentially used to obtain information about molecular gas in galaxies undetectable through emission lines.

Absorption lines also confer the advantage of the ease of follow-up observations in many molecular lines other than CO. Indeed, once a high-column-density absorber has been discovered, the detection of other lines does not suffer from low filling factor – as is the case for emission –, nor critical density for excitation. This enables characterization of the physical and chemical conditions in the absorbing gas (e.g., Henkel et al. 2005; Bottinelli et al. 2009; Muller et al. 2014, 2016, 2021). The relative strengths of species like  $\text{H}_3\text{CN}$ , where the excitation is dominated by the cosmic microwave background (CMB), can be used to determine the CMB temperature (e.g., Henkel et al. 2009; Muller et al. 2013). Comparisons between the redshifts of different transitions (e.g.,  $\text{NH}_3$ ,  $\text{CH}_3\text{OH}$ , OH, etc.) can be used to test for variations in the fundamental constants (e.g., Uzan 2011; Kanekar 2011; Kanekar et al. 2012; Bagdonaite et al. 2013; Murphy et al. 2022).

Absorption-line studies broadly fall in two categories. In cases where the absorbing gas ( $z_{\text{abs}}$ ) is located in the same radio source ( $z_{\text{em}}$ ), i.e., an active galactic nucleus (AGN), the absorber is called an associated absorber ( $z_{\text{abs}} \sim z_{\text{em}}$ ). According to the adopted definition, the relative difference between  $z_{\text{em}}$  and  $z_{\text{abs}}$  may only be lower than  $3000 \text{ km s}^{-1}$  (e.g., Wolfe et al. 1986; Ellison et al. 2002; Gupta et al. 2021). In this category, the absorbing gas may originate from the circumnuclear disk or may represent outflowing or infalling material. In the second category, the absorbing gas is unrelated to the background AGN and arises from an “intervening” galaxy ( $z_{\text{abs}} < z_{\text{em}}$ ). Through high-spatial-resolution observations, the number of associated molecular absorption line detections in the local Universe is steadily increasing (e.g., Tremblay et al. 2016; Rose et al. 2019a,b, 2020). These provide extremely useful information about the gas distribution and kinematics, which can be used, for example, to distinguish inflows from outflows. Two absorbers are also detected at high-redshift: Abell 2390 ( $z = 0.230$ ) and RXC J0439.0+0520 ( $z = 0.208$ ; Rose et al. 2019a); both are associated with the brightest galaxies of the corresponding galaxy cluster.

Molecular absorptions at higher-redshifts are extremely rare. Up to now, only ten molecular absorption systems have been discovered in the mm domain at  $z \gtrsim 0.1$ . Among these, five are intervening molecular absorptions: three are associated with lensing galaxies amplifying the background quasars PKS1830–211, B0218+357 (e.g., Combes 2008), and PMN0134–0931 (Wiklind et al. 2018); the fourth is PKS1413+135 and the last is our recent CO/CN absorption detection in front of the quasar Q0248+430 ( $z_{\text{em}} = 1.31$ ; Combes et al. 2019). The quasar sight line in the latter case is probing the gas associated with the tidal tail emanating from a merging galaxy pair, G0248+430 ( $z = 0.05194$ ), at an impact parameter of  $\sim 15$  kpc. The HI and OH absorptions at centimeter wavelengths have already been detected, revealing the presence of cold atomic and molecular gas toward the sight line (Gupta et al. 2018a), leading to the above-mentioned CO/CN detection with the Northern Extended Millimeter Array (NOEMA).

The five high- $z$  associated absorptions, in addition to the two associated with the brightest cluster galaxies (BCGs) mentioned above, are B3 1504+377 (Combes 2008), 4C+12.50 (Dasyra & Combes 2012), and PKS B1740–517 (Allison et al. 2019). This recent CO detection with the ALMA was motivated by a HI 21 cm absorption detection (Allison et al. 2015).

The CO(3–2) spectrum of 4C+12.50 displays both an emission component at the galaxy redshift  $z=0.1218$  and an absorption feature of  $\sim 1000 \text{ km s}^{-1}$  from it. The latter was interpreted by Dasyra & Combes (2012) as representing outflowing gas. Recently, a search for associated absorption lines was also attempted with the calibrators of ALMA, but with no success (ALMACAL; Klitsch et al. 2019). We also note that it is debatable whether the absorber toward PKS1413+135 is of associated or intervening category (Readhead et al. 2021; Combes et al. 2023). Based on recent advances, here we consider it to be an intervening absorber.

Interestingly, molecular absorptions of  $\text{H}_2$  and CO are relatively easy to detect at high-redshift using ultraviolet (UV) lines (e.g., Petitjean et al. 2000; Srianand et al. 2008; Noterdaeme et al. 2023). The  $\text{H}_2$  detection rates among sight lines selected on the basis of the presence of a DLA ( $N(\text{HI}) > 2 \times 10^{20} \text{ cm}^{-2}$ ) are low ( $\lesssim 10\%$ ).  $\text{H}_2$  is more frequently detected in DLAs with higher metallicity. More importantly, UV lines can detect molecular column densities one or two orders of magnitude lower ( $N(\text{H}_2) \sim 10^{14} \text{ cm}^{-2}$ ) than what is possible with mm lines. But at higher column densities, the background source is obscured by accompanying dust (Noterdaeme et al. 2015). As UV lines are biased against high-column-density molecular gas, the mm absorption lines are a welcome complementary tool (Combes 2008).

We report here a systematic search for CO emission and absorption in a sample of 30 targets selected on the basis of the presence of cold atomic gas already confirmed through the detection of HI 21 cm absorption. This paper is structured as follows. Our sample is described in Sect. 2. Section 3 presents the details of our mm observations using the Institut de Radioastronomie Millimétrique (IRAM)-30 m telescope and NOEMA. The results in terms of optical depth and column density are quantified in Sect. 4. In Sect. 5, we discuss the constraints brought by the negative results on the various absorption components in comparison with the atomic or ionized gas absorptions. Section 6 summarizes our conclusions. Throughout the present paper, the velocity scale is defined with respect to redshifts indicated in Table 1. To compute distances, we adopt a flat  $\Lambda$ CDM cosmology, with  $\Omega_{\text{m}} = 0.29$ ,  $\Omega_{\Lambda} = 0.71$ , and the Hubble constant  $H_0 = 70 \text{ km s}^{-1} \text{ Mpc}^{-1}$ .

## 2. The sample

We gathered a sample of 30 candidates for molecular absorption and emission line search. In all of them, the presence of cold atomic gas has already been confirmed through detection of HI 21 cm absorption (Table 1). Overall, the sample consists of 16 associated systems at the redshift  $z_{\text{abs}} \sim z_{\text{em}}$ , and 14 intervening ones where  $z_{\text{abs}}$  is significantly lower than  $z_{\text{em}}$ . The selected AGNs typically have high ( $>100$  mJy) flux densities at cm wavelengths. The exceptions are J0229+0044 (3.4 mJy) and J0229+0053 (31.1 mJy) from Chowdhury et al. (2020) in which HI 21 cm absorption is still detected due to the presence of large amounts of cold gas. At low- $z$  ( $z \sim 0.1$ ), such high 21 cm optical depths are found to be associated with radio sources embedded in merging galaxy pairs or Ultra Luminous Infrared Galaxies (ULIRGs; Dutta et al. 2019). The basic properties of the sample are presented in Table 1. The absorption redshifts,  $z_{\text{abs}}$ , in Table 1 are based on the peak of HI 21 cm absorption lines, except for PKS 1200+045, where it is the middle of the absorption range; this line is highly blueshifted with respect to the emission redshift. The intervening absorption lines are generally narrow with widths of  $\sim 50 \text{ km s}^{-1}$  and these are therefore observed with

**Table 1.** Properties of the sample – first 16 associated systems and then 14 intervening absorbers are presented.

Target	Other name	$z_{em}$	$z_{abs}$	$\nu_{obs}(1)$ (GHz)	$S_{cont}$ (mJy)	Epoch	HI 21-cm references
(1)	(2)	(3)	(4)	(5)	(6)	(7)	(8)
J000557.17+382015.1	B0003+38A	0.229	0.2288	93.808	900	05–19	Aditya & Kanekar (2018)
J010826.84–003724.1	UM305	1.3753	1.3710	97.232	200	04–21	Gupta et al. (2007)
				112.846 <sup>(a)</sup>		07–10	
J014652.79–015721.2	4C-02.08	0.9590	0.9589	91.059 <sup>(a)</sup>	20	05–19	Aditya (2019)
J022928.93+004429.5	J0229+0044	1.2161	1.2166	104.008	0.5	04–22	Chowdhury et al. (2020)
J022947.23+005308.9	J0229+0053	–	1.1630	106.582	2	04–22	Chowdhury et al. (2020)
J043103.76+203734.2	PKS0428+20	0.219	0.2202	94.469	300	07–10	Vermeulen et al. (2003)
J104830.37+353800.8	B2 1045+35A	0.8464	0.8471	124.811	20	04–21	Aditya (2019)
J120321.93+041419.1	PKS1200+045	1.2243	1.2111	104.263	200	04–21	Aditya & Kanekar (2018)
J124823.89–195918.8	PKS1245–19	1.275	1.2750	101.335	20	04–21	Aditya & Kanekar (2018)
J132616.51+315409.5	4C+32.44	0.3680	0.3680	84.263	1000	07–10	Vermeulen et al. (2003)
J134733.36+121724.2	4C+12.50	0.1217	0.1217	102.765	1500	07–10	Morganti et al. (2004)
J140700.39+282714.7	Mrk668	0.0768	0.0775	106.980	250	07–10	Gupta et al. (2006)
J154015.23–145341.9	J1540–1453	2.104	2.1139	74.035	60	04–21	Gupta et al. (2021)
J164801.53+222433.3	J1648+2224	0.8227	0.8233	126.440	100	04–21	Aditya (2019)
J194553.51+705548.7	1946+708	0.1008	0.1008	104.716	48	06–10	Peck et al. (1999)
J205252.05+363535.3	B2-2050+36	0.354	0.3546	85.096	214	06–10	Vermeulen et al. (2003)
J020346.66+113445.4	PKS0201+113	3.639	3.38714	131.354	100	07–10	Kanekar et al. (2007)
				105.089		07–10	
J025134.54+431515.8	Q0248+430	1.313	0.05151	109.624	150	07–10	Hwang & Chiou (2004) (1)
J074110.70+311200.2	0738+313	0.6310	0.22124	94.389	800	06–10	Kanekar et al. (2001),(2)
J080839.66+495036.5	SBS0804+499	1.4344	1.40732	95.765	200	03–19,07–10	Gupta et al. (2009), (3)
J083052.09+241059.8	0827+243	0.9406	0.52476	75.600	900	06–10	Kanekar & Chengalur (2001), (2)
J092136.24+621552.2	J0921+6215	1.4473	1.10360	109.592	1000	03–19	Dutta et al. (2017), (4)
J095456.82+174331.2	0952+179	1.4749	0.23780	93.126	40	06–10	Kanekar & Chengalur (2001)
J124355.79+404358.9	B3 1241+410	1.5266	0.01714	113.329	80	07–10	Gupta et al. (2018b)
J133335.78+164903.9	HB1331+170	2.0835	1.77646	83.033	500	03–19	Carswell et al. (2011), (2)
J140856.48–075226.5	PKS1406–076	1.494	1.27464	101.351	1500	03–19,06–10	Gupta et al. (2012)
J162439.09+234512.2	3C336	0.9272	0.65584	107.725 <sup>(a)</sup>	100	06–10	Curran et al. (2007)
J163956.36+112758.7	J1639+1127	0.993	0.07909	106.823	70	07–10	Srianand et al. (2013)
J203155.23+121940.4	PKS2029+121	1.215	1.11614	84.293 <sup>(a)</sup>	2000	06–10	Gupta et al. (2012)
J235810.87–102008.7	HB2355–106	1.6349	1.17304	106.090	600	07–10	Gupta et al. (2007), (3)

**Notes.** Columns: (1, 2) object coordinates and favored name; (3, 4) redshift of emission and absorption, the latter is based on the HI 21 cm absorption peak, except for PKS1200+045 (see text for details); (5) observed frequency, CO(1–0) or CO(2–1) except when indicated otherwise; (6) 3 mm continuum flux density in mJy based on the measurements from NED; (7) epoch of IRAM-30 m observations; (8) HI 21 cm absorption references. <sup>(a)</sup>for HCO<sup>+</sup>(2–1) or (3–2).

**References.** (1) Combes et al. (2019), (2) Berg et al. (2015), (3) Quider et al. (2011), (4) Stickel & Kuhr (1993).

spectral resolution of a few km s<sup>−1</sup> (e.g., Gupta et al. 2012). The absorption redshifts of these absorbers in Table 1 have higher accuracy compared to the associated absorbers, which are relatively broader (~100 km s<sup>−1</sup>) and observed with coarser spectral resolution. The interpretation of gas detected in associated absorption crucially depends on the measurement of systemic redshift,  $z_{em}$ , based on optical emission lines. These redshifts are provided in Table 1, and are mostly accurate to four decimal places. We discuss these in detail in Sect. 4.

Based on radio morphology and spectral energy distribution (SED) at cm wavelengths, the associated targets can be classified as compact radio sources (<15 kpc) expanding through the host galaxy ISM (O’Dea & Saikia 2021). The expected values of radio continuum at 3 mm are taken from the NASA Extragalactic Database (NED). As many AGNs have variable fluxes, these are certainly only approximate. The flux densities from our mm observations, which are presented in the following tables, are also uncertain because these are obtained with a single-dish and through a varying atmosphere. The atmospheric contribution is best subtracted though rapid wobbling; however, it remains problematic in average weather conditions.

We searched for molecular absorption at the lowest possible frequency to maximize the continuum brightness level, and hence the detectability of absorption. All sources have been observed in CO lines and according to their redshift HCO<sup>+</sup> lines when possible. Our goal is to detect CO in emission or absorption and high-density tracers simultaneously, such as HCO<sup>+</sup> or HCN, which become diffuse gas tracers in absorption. We note that some of the associated absorbers from the sample have been followed up to search for the OH line in absorption, namely with MeerKAT through the approved large program – the MeerKAT Absorption Line Survey (MALS<sup>1</sup>; Gupta et al. 2016, 2021).

### 3. Observations and data analysis

All the targets were first observed with the IRAM-30 m telescope at Pico Veleta, Granada, Spain, at the epochs indicated in Table 1. The lines observed were mainly either CO(1–0) or CO(2–1) at 3 mm and CO(3–2) at 2 mm, except in some cases HCO<sup>+</sup>(2–1) or (3–2). The full width at half maximum

<sup>1</sup> <https://mals.iucaa.in/>

(FWHM) of the primary beams at the frequencies of 100 GHz and 150 GHz are  $25''$  and  $17''$ , respectively. The SIS receivers (EMIR) were used for observations in the wobblers switching mode, with reference positions offset by  $\pm 60$  arcsec in azimuth. The efficiency of the main beam of IRAM is  $\eta_{\text{mb}} = T_{\text{A}}^*/T_{\text{mb}} = 0.84$  and  $0.78$  at 100 GHz and 150 GHz, respectively. The system temperatures ranged between 120 K and 220 K at 3 mm, and between 180 K and 300 K at 2 mm. The pointing accuracy was checked every 2 h on a nearby planet or a bright continuum source, and the focus was reviewed after each sunrise, as well as at the beginning of each night. The integration time is typically 2 h per source, and is weather-dependent. Two backends were used simultaneously, the wideband autocorrelator, WILMA, and the Fourier Transform Spectrometer (FTS). Their respective spectral resolutions are 2 MHz and 0.2 MHz, which correspond to 6 and  $0.6 \text{ km s}^{-1}$  at 3 mm. The rms noise levels at 100 GHz and 150 GHz for a velocity resolution of  $40 \text{ km s}^{-1}$  were  $\sigma \sim 1.0 \text{ mK}$  and  $1.3 \text{ mK}$  in  $T_{\text{A}}^*$ , respectively. The data were reduced using the Continuum and Line Analysis Single-dish Software (CLASS) of the Grenoble Image and Line Data Analysis Software (GILDAS).

For two sources detected in line emission, PKS 1200+045 and PKS 1245–19, further observations in the 3 mm band were carried out with NOEMA using the PolyFIX correlator in February, March, and November, 2022. The CO(2–1) line at  $z = 1.226$  (PKS 1200+045) and  $1.275$  (PKS 1245–19) is redshifted to 103.566 and 101.335 GHz, respectively. The observations were carried out in dual polarisation mode in four base bands, with 3.9 GHz total bandwidth per baseband, distributed in lower and upper sidebands distant by 15.5 GHz. The CO(2–1) line was observed in the upper side band. We observed 80% of the time in A-configuration, and 20% in C-configuration, with 12 antennas. The total telescope time per source was 13 h (8 h on source), with a total of 26 h. The calibrations were performed using strong radio sources, such as 3C273, 3C84, 1222+037, and 1244–255. The absolute flux calibration is accurate at the 10% level.

The data were calibrated using the Continuum and Line Interferometer Calibration (CLIC) package and mapped using the MAPPING package of the GILDAS software. We used self-calibration, which significantly increased the signal-to-noise ratio. Using CLARK cleaning with natural weighting, we obtained images with synthesized beams of  $6''.9 \times 1''.3$  (PKS 1200+045) and  $4''.1 \times 1''.2$  (PKS 1245–19) with a position angle (PA) of  $10^\circ$ . As no other lines were detected in the rest of the base bands (upper and lower), we used these to estimate and subtract the continuum level. The velocity resolution was initially 2 MHz ( $\sim 6 \text{ km s}^{-1}$ ). The data were then smoothed to obtain data cubes with three resolutions: 10, 50, and  $150 \text{ km s}^{-1}$ . These final cubes are  $256 \times 256$  pixels with  $0.13''$  per pixel in the plane of the sky, and have 80 frequency channels. The continuum flux density was also computed using the images from the wider 7.7 GHz lower side band, with a beam of  $7''.1 \times 1''.4$  or  $4''.9 \times 1''.4$ , with a PA of  $10^\circ$ . The rms noise is  $230 \mu\text{Jy beam}^{-1}$  in  $50 \text{ km s}^{-1}$  channels for the line and  $10 \mu\text{Jy beam}^{-1}$  for the continuum.

## 4. Results

In Sect. 4.1, we first discuss the emission and then absorption line detections from IRAM-30 m observations. The results from NOEMA interferometer follow-up observations of associated systems PKS 1200+045 and PKS 1245–19 are presented in Sect. 4.2.

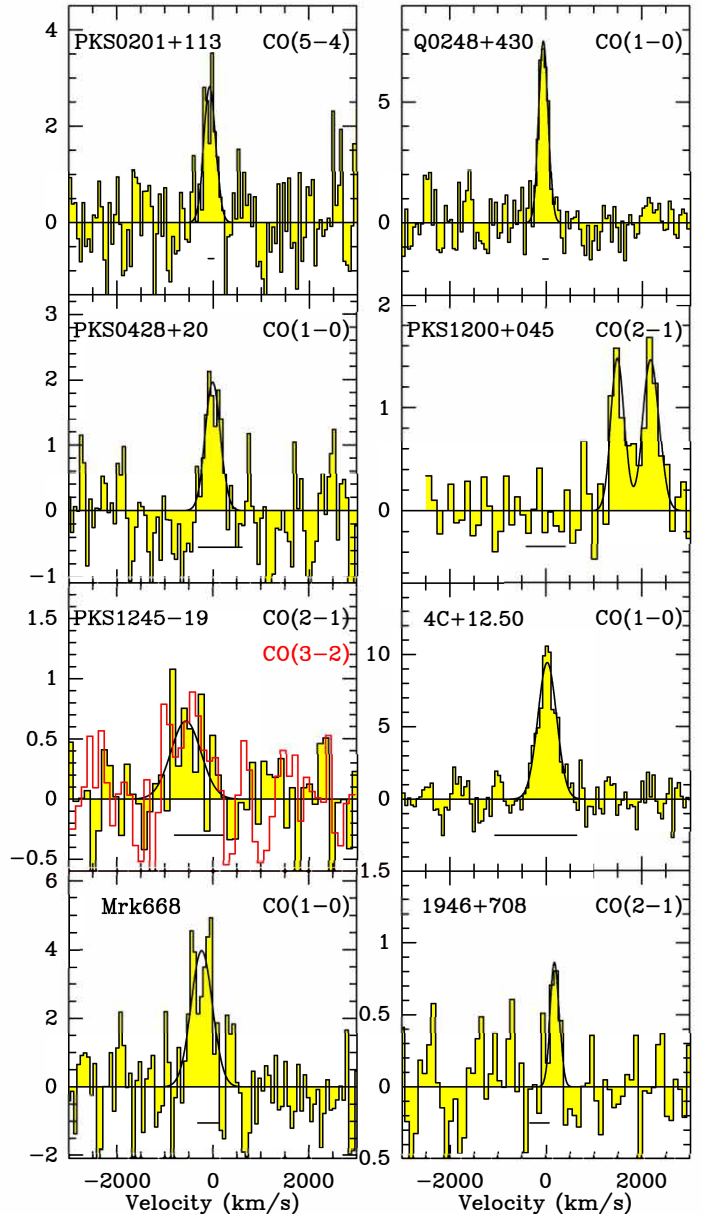


**Fig. 1.** Detection of CO emission lines toward two intervening (top panels) and six associated absorbers obtained with the IRAM-30 m. The vertical scale is  $T_{\text{mb}}$  in mK. The various CO transitions are indicated at the upper right of each panel. The zero of the velocity scale corresponds to  $z_{\text{abs}}$  in Table 1. The velocity range over which HI 21 cm absorption is detected is indicated by an horizontal bar at the bottom of each panel. The detection toward 1946+708 is only tentative.

### 4.1. IRAM-30 m

#### 4.1.1. Emission

Figure 1 displays profiles of CO emission lines detected toward eight of the targets with the IRAM-30 m telescope. We note that the detection toward 1946+708 is only tentative. Of these eight, two correspond to intervening HI 21 cm absorbers and the remaining to the associated absorbers (see also Table 2). The detections toward Q0248+430 (J0251+4315; Downes et al. 1993), 4C+12.50 (J1347+1217; Dasyra & Combes 2012), and Mrk 668 (J1407+2827; Ocaña Flaquer et al. 2010) were

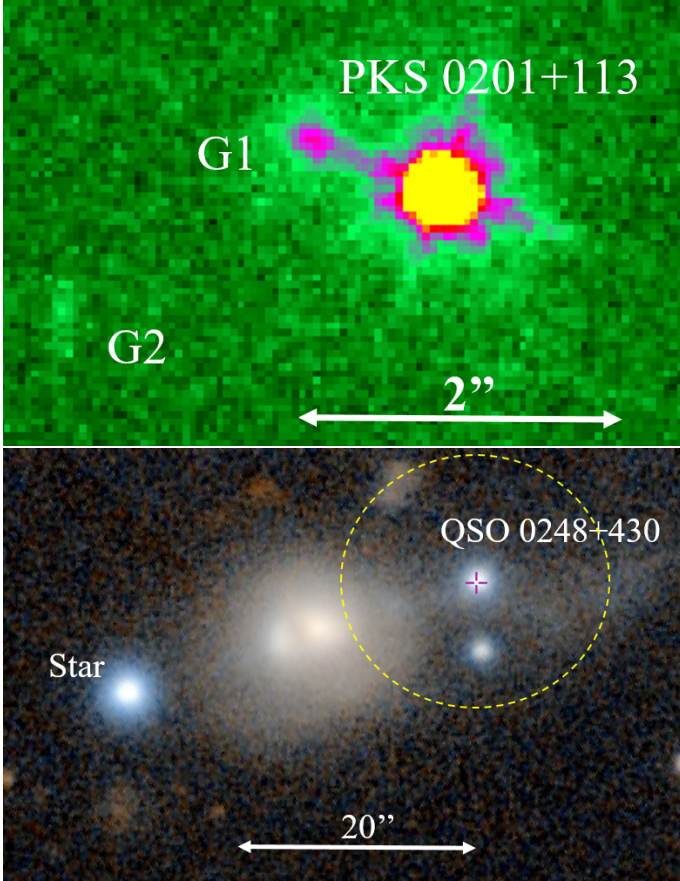


**Fig. 2.** QSO-galaxy pairs detected in CO emission and absorption. Top: HST-*F606W* image of PKS0201+113, with the galaxies G1 and G2; the latter is considered the most likely DLA candidate by Ellison et al. (2001). Bottom: PanSTARRS1 three-color ( $z - z_g - g$ ) image of Q0248+430 and associated galaxies. The dashed yellow circle indicates the region observed with the 23'' beam.

previously known, and the remaining are reported here for the first time.

The two intervening systems detected in CO emission are toward PKS0201+113 (J0203+1134) and Q0248+430 (J0251+4315). Although both can be classified as QSO-galaxy pairs (QGP; i.e., a foreground galaxy producing absorption in the sight line of a distant quasar as shown in Fig. 2), the absorber toward PKS0201+113 was first identified as a DLA at  $z_{\text{abs}} = 3.38639$  (White et al. 1993) and was then subsequently associated to a foreground concentration of galaxies, with one of them producing the absorption (Ellison et al. 2001). The absorber galaxy responsible for the DLA may be G2 in Fig. 2. It is relatively massive ( $0.7L^*$ ) and at an impact parameter of  $\sim 20$  kpc. The DLA with  $N(\text{H I}) = 10^{21.26 \pm 0.08} \text{ cm}^{-2}$  exhibits multiple components spread over  $\sim 270 \text{ km s}^{-1}$ . The H I 21 cm absorption exhibits two components spread over  $\sim 115 \text{ km s}^{-1}$  at  $z_{\text{abs}} = 3.387144(17)$  and  $3.386141(45)$  (Kanekar et al. 2007). The  $z_{\text{abs}}$  adopted in Table 1 corresponds to the peak of stronger 21 cm absorption component. The 21 cm absorption peaks do not coincide with the metal and H<sub>2</sub> absorption lines detected in the optical/UV spectra (Ellison et al. 2001; Kanekar et al. 2007; Srianand et al. 2012). The CO emission spectrum is in good correspondence with the velocity range over which [Fe II], [C II], and H<sub>2</sub> absorption lines are detected (Srianand et al. 2012).

Being closer ( $z \sim 0.05$ ), the merging galaxy pair in front of the quasar Q0248+430 (J0251+4315) at  $z = 1.313$

has been detected in several CO emission lines (Kuehr 1977; Kollatschny et al. 1991). The CO(1–0) integrated flux density ( $S_{\text{CO}dV}$ ) using the Berkeley-Illinois-Maryland Association (BIMA) interferometer was  $24 \text{ Jy km s}^{-1}$  (Hwang & Chiou 2004). With the IRAM-30 m, Downes et al. (1993) reported  $S_{\text{CO}dV} = 25 \text{ Jy km s}^{-1}$ , while from our observations we estimate  $S_{\text{CO}dV} = 8.5 \text{ Jy km s}^{-1}$ . However, in our observations, the telescope was pointed toward the QSO, which is about 15'' from the foreground galaxy. Combes et al. (2019), using NOEMA observations, showed that the CO emission is confined to the few central arcseconds of the galaxy. Therefore, the telescope beam only partially covers the CO emission region associated with the galaxy, as shown in Fig. 2, which explains the discrepancy with earlier observations. We note that the tidal tail emanating from the foreground galaxy extends across the background QSO and is responsible for the CO absorption line detection (Combes et al. 2019). Unlike the case of PKS0201+113, the molecular absorption in this case is coincident with the narrower and stronger H I 21 cm absorption components (see also Gupta et al. 2018a).

Among six associated molecular-emission-line detections, the four lower-redshift detections are associated either with radio or Seyfert (Sy) galaxies (see Table 2). 4C+12.50 (J1347+1217) is associated with a merging galaxy pair at  $z = 0.12174 \pm 0.00002$  (Holt et al. 2003), with infrared luminosity of  $3.2 \times 10^{12} L_{\odot}$  (Scoville et al. 2000). This has been detected in CO in emission as well as absorption (Dasyra & Combes 2012; Dasyra et al. 2014). An image of the associated galaxy pair can be seen in Fig. 5 of Dasyra et al. (2014). The host of Mrk 668 (J1407+2827; OQ208) is an actively star forming galaxy, with an interacting companion (see Fig. 3), at  $z = 0.07681 \pm 0.00007$  (Eracleous & Halpern 2004). It was detected previously by Ocaña Flaquer et al. (2010) in CO(1–0) and also shows stimulated radio-recombination lines (Bell & Seaquist 1980). Due to its far-infrared luminosity of  $2 \times 10^{11} L_{\odot}$ , it is classified as a LIRG. 1946+708 (J1945+7055) is a radio galaxy at  $z = 0.10083 \pm 0.00009$  (Snellen et al. 2003). PKS0428+20 (J0431+2037), also a radio galaxy, has a redshift measurement of  $z = 0.219$  with modest accuracy (Labiano et al. 2007).

The two higher-redshift associated detections are PKS1200+045 (J1203+0414) and PKS1245–19 (J1248–1959) at  $z = 1.22429 \pm 0.00043$  (Shen et al. 2011; Aditya & Kanekar 2018) and 1.275 (Labiano et al. 2007), respectively. For PKS1200+045, the double-peaked CO emission profile agrees with the optical redshift within  $1\sigma$ . The H I 21 cm absorption is blueshifted with respect to this by  $\sim 2000 \text{ km s}^{-1}$  and has no overlap with the molecular gas. In contrast, for PKS1245–19, the H I 21 cm absorption and CO emission line peaks are consistent within the random and systematic errors of measurements with the systemic redshift based on optical emission lines. In general, except for PKS1200+045, for all the associated systems, the H I 21 cm absorption is detected within the same velocity range as the CO emission (see horizontal bars in Fig. 1).

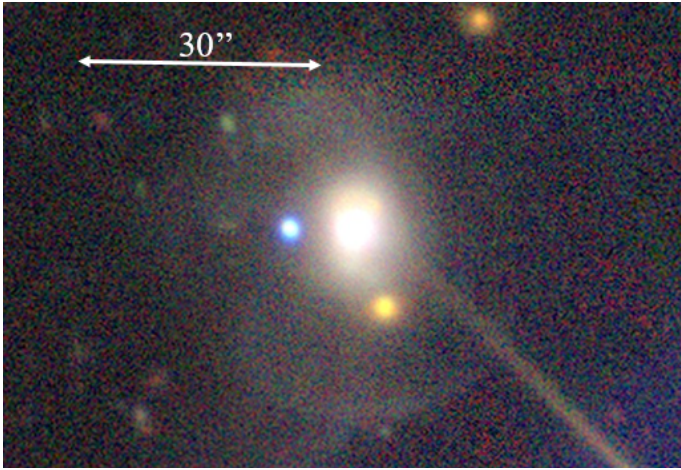
We compute  $L'_{\text{CO}}$ , the CO luminosity in units of  $\text{K km s}^{-1} \text{ pc}^2$ , with the integrated emission in the beam. This CO luminosity is given by

$$L'_{\text{CO}} = 3.25 \times 10^7 S_{\text{CO}dV} \frac{D_L^2}{v_{\text{rest}}^2 (1+z)} \text{ K km s}^{-1} \text{ pc}^2, \quad (1)$$

where  $S_{\text{CO}dV}$  is the integrated flux in  $\text{Jy km s}^{-1}$ ,  $v_{\text{rest}}$  is the rest frequency in GHz, and  $D_L$  is the luminosity distance in megaparsecs. Under the assumption of a standard CO-to-H<sub>2</sub> conversion factor (Bolatto et al. 2013), we compute the H<sub>2</sub> mass using

**Table 2.** Detection of CO emission in two intervening systems, PKS0201+113 and Q0248+430, and six associated systems.

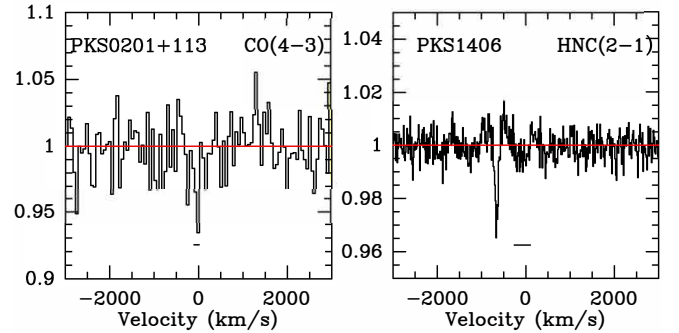
Target	$z_{\text{mol}}$	CO	$S_{\text{peak}}$ (mJy)	$FWHM$ ( $\text{km s}^{-1}$ )	$M(\text{H}_2)$ ( $10^9 M_{\odot}$ )	Optical Id.	Radio Id.	$\log L_{1.4\text{GHz}}$ ( $\text{W Hz}^{-1}$ )
(1)	(2)	(3)	(4)	(5)	(6)	(7)	(8)	(9)
PKS0201+113	3.38715	5–4	$11 \pm 3$	$289 \pm 50$	768	–	–	–
Q0248+430	0.05151	1–0	$38 \pm 5$	$225 \pm 23$	5	–	–	–
PKS0428+20	0.22020	1–0	$10 \pm 2$	$368 \pm 64$	40	G	GPS	26.6
PKS1200+045	1.22216	2–1	$6.4 \pm 1$	$750 \pm 90$	488	Q	GPS	27.9
PKS1245–19	1.27121	2–1	$3.7 \pm 1$	$752 \pm 140$	327	Q	GPS	28.6
	1.27121	3–2	$3 \pm 1.5$	$733 \pm 180$	190			
4C+12.50	0.12170	1–0	$47 \pm 5$	$457 \pm 32$	71	Sy/Q	CSS	26.3
Mrk 668	0.07642	1–0	$20 \pm 5$	$521 \pm 69$	13	Sy	GPS	24.9
1946+708	0.10147	2–1	$4.3 \pm 1$	$222 \pm 90$	0.6	G	GPS	25.3

**Notes.** Columns: (1) favored name; (2)  $z$  of the CO emission peak; (3) CO transition; (4, 5) emission line peak and FWHM; (6) molecular mass; (7, 8) optical and radio identifications (GPS: GHz-peaked spectrum, CSS: compact steep spectrum), and 1.4 GHz luminosity for associated systems.**Fig. 3.** Mrk668 (OQ208, J1407+282) legacy DR9 image, showing an interacting galaxy with stellar shells.

$M_{\text{H}_2} = \alpha L'_{\text{CO}}$ , with  $\alpha = 4.36 M_{\odot} (\text{K km s}^{-1} \text{pc}^2)^{-1}$ . We use a constant conversion factor for the sake of comparison, although the factor could depend on the starbursting character and on the metallicity of galaxies, but we have no information about them. The observation of the fundamental CO(1–0) line is the best measure of the total  $\text{H}_2$  mass. To convert the CO luminosities measured at a  $J$ -level of higher than one, we adopted the  $R_{1J} = T_1/T_J$  ratios from several works in the literature (e.g., Weiß et al. 2007; Dannerbauer et al. 2009; Tacconi et al. 2018), i.e.,  $R_{12} = 1.16$ ,  $R_{13} = 1.8$ ,  $R_{15} = 2.9$ . The molecular gas mass estimates for eight detections are presented in Table 2.

#### 4.1.2. Absorption

Figure 4 shows the spectra of the two molecular-absorption-line detections. They are both intervening systems. The values of continuum flux density, optical depth, and column density are provided in Table 3. PKS0201+113 exhibits a weak absorption ( $\sim 3\sigma$ ) in the CO(4–3) line, and the detection is only tentative. The absorbing galaxy is also detected in emission in CO(5–4) (see Fig. 1). The continuum flux density of the quasar is a factor of two higher at the lower frequency of the CO(4–3) line with respect to the higher frequency of CO(5–4). At the latter

**Fig. 4.** Absorption features observed with the IRAM-30 m toward two of the intervening targets PKS0201+113 in CO(4–3) on the left, and PKS1406–076 in HNC(2–1) on the right. The detection toward PKS0201+113 is only tentative. The spectra have been normalized to their continuum flux densities of 0.22 and 1.13 Jy, respectively. The zero on the velocity scale corresponds to the peak of HI 21 cm absorption ( $z_{\text{abs}}$  in Table 1). The velocity range over which HI absorption is detected is indicated by a horizontal bar at the bottom of each panel. For PKS0201+113, the  $\text{H}_2$  absorption peak ( $-25 \text{ km s}^{-1}$ ) and the velocity range over which the 21 cm ( $-100, 10 \text{ km s}^{-1}$ ) and the [CII]\* ( $-80, 0 \text{ km s}^{-1}$ ) are detected are reasonably consistent with the CO absorption (see text for details).

frequency, the absorption signal is weak and does not compensate for the emission. The contrary is true at the CO(4–3) frequency: the absorption signal is stronger and cancels out the emission. The CO(4–3) absorption coincides well with the velocity range ( $-100, 10 \text{ km s}^{-1}$ ) over which the HI 21 cm absorption is detected. However, we note that the peaks of 21 cm and  $\text{H}_2$  absorption lines, despite both being tracers of cold gas, are disparate by  $\sim 25 \text{ km s}^{-1}$  (Srianand et al. 2012). The differences in absorption line velocities are most likely due to the nonalignment of radio and optical sight lines. The radio core, especially at cm wavelengths, is also more extended than the astronomical unit (au)-sized optical quasar and probes a larger volume of the absorbing gas.

PKS1406–076 was observed in June 2010 at 101.322 GHz and 151.978 GHz corresponding to the CO(2–1) and CO(3–2) lines redshifted at  $z = 1.2753$ , respectively. The HI 21 cm absorption peak is at  $-87 \text{ km s}^{-1}$  with respect to  $z = 1.2753$ , corresponding to the Mg II absorption. The observation led only to upper limits – with a spectral rms of 8 mJy per channel of  $20 \text{ km s}^{-1}$  – along with rippled baselines, which are likely due

**Table 3.** Details of molecular-absorption-line detections in two intervening and then two associated systems with IRAM-30 m and NOEMA, respectively.

Target	$z_{mol}$	Line	$S_{cont}$ (Jy)	$\int \tau dV$ (km s <sup>-1</sup> )	$N$ (cm <sup>-2</sup> )
(1)	(2)	(3)	(4)	(5)	(6)
0201+113	3.38715	CO43	0.22	6.2 ± 2	6.6E16
1406-076	1.26949	HNC21	1.13	2.4 ± 0.2	2.8E13
1200+045	1.21276	CO21	0.058	3.1 ± 0.6	1.5E16
1245-19	1.26605	CO21	0.067	7.2 ± 0.4	3.6E16

**Notes.** Columns: (1) favored PKS name of the target; (2)  $z$  of the molecular line peak; (3) molecular line transition; (4) continuum flux density; (5) integrated optical depth; and (6) total column density of CO or HNC.

to the high continuum flux density (1.1 Jy). In March 2019, the target was observed again but only in the 3 mm band with a wide configuration, which included CO(2-1) at 101.322 GHz in the upper-outer sideband, but also HNC(2-1) and HCO<sup>+</sup>(2-1) at 79.693 GHz and 78.396 GHz in the lower-outer sideband, respectively. An absorption line was detected near the HNC(2-1) frequency but blueshifted by ~600 km s<sup>-1</sup> with respect to the peak of the 21 cm absorption. The HCO<sup>+</sup>(2-1) frequency was at the edge of the band and suffered from a rippled baseline.

The continuum flux densities and upper limits for nondetections are presented in Table 4. The spectral rms ( $\sigma$ ) is estimated for 20 km s<sup>-1</sup> channels. When the continuum is insufficiently strong, that is, regarding the CO line in particular, the emission line upper limit may be estimated using the rms derived over 80 km s<sup>-1</sup> channels obtained by dividing  $\sigma$  in Table 4 by a factor 2. We do not report all the simultaneously observed lines, but only those offering the greatest constraints are considered here.

Assuming a homogeneous and optically thin gas at excitation temperature  $T_x$  and with a covering factor  $f_c$ , we can derive the average column density over the beam corresponding to the mm continuum emission of the quasar through

$$N_{tot} = \frac{8\pi}{c^3} \frac{\nu^3}{g_J A_{J,J+1}} f(T_x) \int \tau dv, \quad (2)$$

where  $g_J$  is the statistical weight of level  $J$ ,  $A_{J,J+1}$  is the Einstein coefficient for transition  $J \rightarrow J+1$ , and the function  $f(T_x)$  is

$$f(T_x) = \frac{Q(T_x) e^{E_J/kT_x}}{1 - e^{-h\nu/kT_x}}. \quad (3)$$

We adopt the partition function of local thermal equilibrium (LTE), that is,  $Q(T_x) = \sum g_J e^{-E_J/kT_x}$ , where  $E_J$  is the energy of level  $J$  and  $T_x$  is the excitation temperature of the CO molecule.

Typically, with our integration time of 2 h per source, at 3 mm we get an rms of 5 mJy in 20 km s<sup>-1</sup> channels. According to the background radio source flux, between 100 and 300 mJy of continuum, this leads to a  $1\sigma$  upper limit of  $\sim 1.7 \times 10^{-2}$  to  $5 \times 10^{-2}$  in the optical depth  $\tau$ , and  $\tau \Delta V = 0.34$  to  $1 \text{ km s}^{-1}$  at  $1\sigma$  for a line width of  $\Delta V = 20 \text{ km s}^{-1}$ . When the observed line is CO(2-1) or HCO<sup>+</sup>(2-1), this corresponds to  $N(\text{CO}) = 1.6\text{--}5 \times 10^{15} \text{ cm}^{-2}$ , and  $N(\text{H}_2) = 1.6\text{--}5 \times 10^{19} \text{ cm}^{-2}$ , or  $N(\text{HCO}^+) = 2.6\text{--}8 \times 10^{12} \text{ cm}^{-2}$  respectively, assuming an average excitation temperature of  $T_x = 15 \text{ K}$ , and a filling factor of  $f_c = 1$ . We adopt a typical CO/H<sub>2</sub> abundance ratio of  $10^{-4}$  (e.g., Rachford et al. 2009).

The column-density estimates for the two intervening detections with IRAM-30 m are provided in Table 3. We note that,

**Table 4.** Continuum flux densities and line upper limits based on IRAM-30 m for the associated (top) and then intervening systems (bottom).

Target	$\nu_{obs}$ (GHz)	$S_{cont}$ (mJy)	Line	$\sigma$ (mJy)
B0003+38A	93.808	90	CO(1-0)	7
UM305	97.232	120	CO(2-1)	12
	112.846	100	HCO <sup>+</sup> (3-2)	15
4C-02.08	91.059	20	HCO <sup>+</sup> (2-1)	4.5
J0229+0044	104.008	10	CO(2-1)	2.5
J0229+0053	106.582	5	CO(2-1)	3.5
B2 1045+35A	96.570	45	HCO <sup>+</sup> (2-1)	3.5
	124.811	30	CO(2-1)	6
4C+32.44	84.263	240	CO(1-0)	9
J1540-1453	74.035	25	CO(2-1)	7
J1648+2224	126.440	175	CO(2-1)	5
B2-2050+36	85.096	80	CO(1-0)	2.5
0738+313	94.389	370	CO(1-0)	3.5
SBS0804+499	95.765	440	CO(2-1)	12
0827+243	151.196	610	CO(2-1)	5
J0921+6215	109.592	850	CO(2-1)	7
0952+179	93.126	200	CO(1-0) <sup>(a)</sup>	3.5
B3 1241+410	113.329	40	CO(1-0)	10
HB1331+170	83.033	100	CO(2-1)	2.5
3C336	107.725	25	HCO <sup>+</sup> (2-1)	5
	139.227	15	CO(2-1)	3.5
J1639+1127	106.823	340	CO(1-0)	10
PKS2029+121	84.293	900	HCO <sup>+</sup> (2-1)	4
	163.409	505	CO(3-2)	5
HB2355-106	106.090	490	CO(2-1)	4.5

**Notes.** The spectral rms ( $\sigma$ ) is based on 20 km s<sup>-1</sup> channels. <sup>(a)</sup>CO(4-3) detected by ALMA at  $z_{em}$  (Audibert et al. 2022).

although the column density does not depend on redshift, the excitation temperature must nevertheless be higher than the CMB temperature, which is already 12 K for PKS0201+113. When the assumed  $T_x$  is 20K, instead of 15 K, the column density decreases only slightly (13%) for CO(4-3), and increases by 53% for HNC(2-1). For a typical CO/H<sub>2</sub> abundance ratio of  $10^{-4}$ , the H<sub>2</sub> column density is  $N(\text{H}_2) = 6.6 \times 10^{20} \text{ cm}^{-2}$  for PKS 0201+113. This is quite comparable to the H I column density of  $1.8 \times 10^{21} \text{ cm}^{-2}$  derived by Ellison et al. (2001) and Kanekar et al. (2007), from the Lyman- $\alpha$  and H I 21 cm, respectively. For PKS1406-076, we can estimate the abundance of HCN and HNC in the diffuse medium of the Milky Way in absorption in front of background radio sources (Liszt & Lucas 2001) as HCN/H<sub>2</sub> =  $1.4 \times 10^{-9}$  and HNC/HCN = 0.2. The H<sub>2</sub> column density is then  $N(\text{H}_2) = 10^{23} \text{ cm}^{-2}$ .

#### 4.2. NOEMA

The two sources PKS 1200+045 and PKS 1245-19 are clearly detected in 3 mm continuum emission (see Fig. 5). The CO emission lines are also detected, as shown in Figs. 6 and 7, but with much lower amplitude than in the IRAM-30 m spectra. Also for PKS 1200+045 the line shape is different and is blueshifted by ~1000 km s<sup>-1</sup>; it is therefore doubtful. The difference might also be due to extended CO emission being resolved out by the limited  $uv$ -coverage of the interferometer. However, as the smallest extent of the synthesized beam is ~1'' or ~8 kpc, this seems

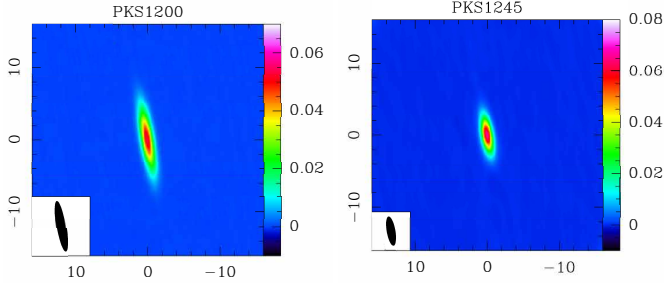


**Fig. 5.** Left: continuum image of PKS1200+045 at 3 mm obtained with NOEMA. Only a 1.5 GHz band has been used around the line frequency to better subtract the continuum. The synthesized beam is  $6''.9 \times 1''.3$ , with PA =  $10^\circ$ . The compact source has a flux density of 58 mJy and detected at S/N of 303. Right: same as above but for PKS1245–19. The synthesized beam is  $4''.1 \times 1''.2$ , with PA =  $10^\circ$ . The compact source has a flux density of 67 mJy (S/N = 421). In both the panels, the spatial scale is in arcseconds and the color bar is in  $\text{Jy beam}^{-1}$ .

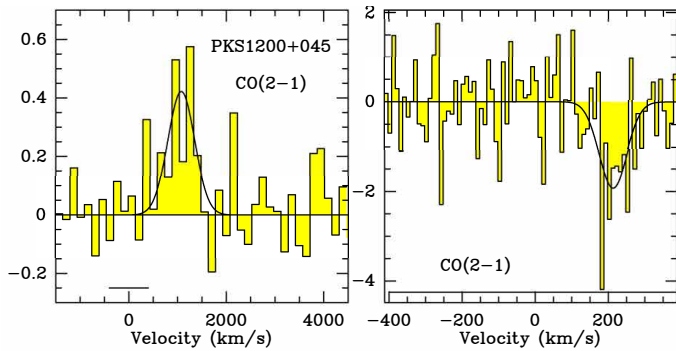


**Fig. 6.** Left: CO(2–1) emission spectrum of PKS1200+045 obtained with NOEMA and smoothed to  $150 \text{ km s}^{-1}$ . The velocity scale is centered at the average of HI absorption. Right: CO(2–1) absorption spectrum toward PKS1200+045. The spectral resolution is  $10 \text{ km s}^{-1}$ . In both panels, vertical scales are in  $\text{mJy beam}^{-1}$  and the horizontal line at the bottom indicates the velocity range over which the HI 21 cm absorption is detected (Aditya & Kanekar 2018).

unrealistic. Another possibility is that the dynamic range is limited to detect weak line emission in the presence of a strong continuum source. Indeed, the intensity of the latter was found to vary significantly within the baseband, affecting the accuracy of the subtraction of the continuum. Computed over the lower and upper sidebands ( $\sim 20 \text{ GHz}$ ), the spectral index of the source is close to  $-1$ ,  $-0.6$  for PKS 1200+045, and  $-1.5$  for PKS 1245–19.

We also detect the CO(2–1) absorption lines in both sources. At  $V = -1803 \text{ km s}^{-1}$  with respect to the optical redshift, the molecular absorption is consistent with the velocity range over which the HI 21 cm absorption is detected by Aditya & Kanekar (2018). The absorption peaks are shifted by  $\sim 200 \text{ km s}^{-1}$  and the molecular line overlaps with the weaker, shallower HI absorption component. For PKS 1245–19, the molecular absorption line peak is at  $V = -1180 \text{ km s}^{-1}$  with respect to the optical redshift, that is, the edge of the blueshifted wing of the HI 21 cm absorption (Aditya & Kanekar 2018). Although the CO(2–1) absorption associated with PKS 1245–19 appears very deep in the NOEMA spectrum, it is not incompatible with the non-detection in the IRAM-30 m spectrum: the peak of the absorption is  $-4 \text{ mJy}$ , and the spectral rms in the IRAM-30 m spectrum is  $2.5 \text{ mJy per } 50 \text{ km s}^{-1} \text{ channel}$ .

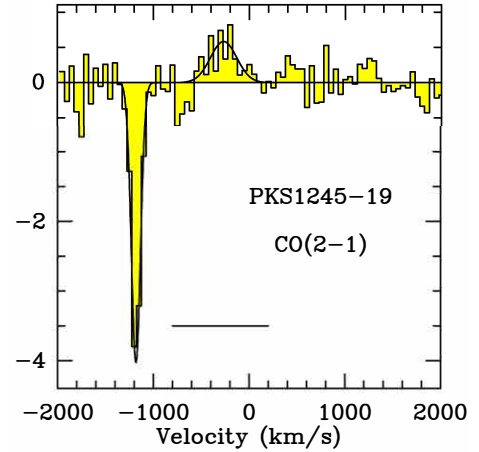


**Fig. 7.** CO(2–1) emission and absorption spectrum of PKS1245–19 obtained with NOEMA and smoothed to  $150 \text{ km s}^{-1}$ . The vertical scale is  $\text{mJy beam}^{-1}$ . The horizontal line at the bottom indicates the velocity range over which the HI 21 cm absorption is detected (Aditya & Kanekar 2018).

## 5. Discussion

The rarity of molecular absorptions among systems with HI 21 cm absorption (5 out of 30) – even when the mm continuum is sufficiently strong and the CO emission line is detected – might appear surprising. But this is likely the consequence of the low surface filling factor ( $f_s$ ) of the molecular gas. There may be molecular gas along the line of sight, with a rather wide beam of 10 kpc scales, as seen in the cases with CO emission, but the surface may be filled at  $f_s \sim 1\%$  or lower (Wiklind & Combes 1997). In contrast, the filling factor of the atomic gas is higher for the same column density. In addition, radio continuum emission is more extended at cm wavelengths than at mm wavelengths. Both these factors lead to more favorable conditions for the detection of cold atomic gas in absorption at longer wavelengths than molecular gas at mm wavelengths.

When the CO lines are detected in emission, higher-spatial-resolution observations are required to isolate the compact nuclear continuum emission and avoid a situation where the emission line outshines the absorption signal. NOEMA was used for two of the associated systems detected in emission. Although the continuum is strongly detected, the absorption signal is rather weak. The detection of weak absorption signals is made even more difficult by the influence of strong continuum emission on the noise level and the baseline stability.

Alternatively, it is possible to detect absorption in the high-density tracers, such as  $\text{HCO}^+$ , HCN, and HNC, which are not detectable in emission. This is indeed the case for the intervening system toward PKS1406–076.

The eight CO emission line detections in our sample correspond to  $M(\text{H}_2) = 10^9 - 7 \times 10^{11} M_\odot$ . Six of these are associated systems and the majority (i.e., four) are at low redshift ( $z < 0.25$ ). Among intervening systems, one detection is at  $z = 3.3871$  and the other at 0.05151. It is interesting to stack all the nondetection spectra listed in Table 4 by aligning these to the same velocity scale centered at the peak of the HI 21 cm absorption. We stacked these spectra with no particular weight related to continuum level or redshift; simply taking into account their rms. The latter was comparable for all sources, and therefore no individual one dominates. The stacked spectrum in Fig. 8 reveals a weak emission. The FWHM of the feature is rather

large ( $870 \text{ km s}^{-1}$ ), and is most likely due to nonalignment of the H I absorption with the systemic velocity of the galaxies. The integrated flux is  $1.75 \pm 0.3 \text{ Jy km s}^{-1}$ . We also stacked the associated and intervening nondetections separately, but the resulting spectra do not show any detectable feature.

### 5.1. Comparison of H I and H<sub>2</sub> column densities

We compared the atomic and molecular column densities of 14 known high-redshift ( $z > 0.1$ ) *molecular-absorption-line* systems. Table 5 provides a compilation of their basic properties from the literature. Seven of these are associated targets. One of these is not detected in H I 21 cm absorption, although the upper limit is quite shallow. In order to estimate molecular column densities, the excitation temperature was adopted from the original reference when physically justified, or was taken as the default,  $T_x = 15 \text{ K}$ , for CO. Estimating the spin temperature for H I is more problematic. For intervening absorbers, based on the Milky Way ISM, a value of 100 K is generally taken. The spin temperature may be at least as high as 1000 K in the associated absorbers (e.g., Maloney et al. 1996). In Table 5, we adopt  $T_s = 1000$  and 100 K for associated and intervening absorbers, respectively. Figure 9 shows H I and H<sub>2</sub> column densities for both types of systems. Clearly, there is no correlation when the bias of higher absorption depth at greater distances (i.e., at higher  $z$ ) is taken into account; emission is more difficult to detect and only absorption may be detected. The  $N(\text{H}_2)/N(\text{H I})$  ratio is in the range of 0.03–2.7 for the associated systems; for the intervening systems, it is 0.2–1000, with the top three (22–1000) corresponding to the lensed systems.

The scatter decreases if we adopt  $T_s = 100 \text{ K}$  for both the associated and intervening systems. However, a uniform spin temperature for both types of systems cannot be justified simply on the basis of H<sub>2</sub>/H I ratios. The associated systems exhibit broader lines, with a median FWHM of  $\sim 150 \text{ km s}^{-1}$  in H I and – as discussed in Sect. 5.3 – comprise gas from two distinct components: the circumnuclear disk and the galaxy-wide ISM. On the other hand, for the intervening H I absorption lines are narrower ( $\text{FWHM} \sim 40 \text{ km s}^{-1}$ ) and represent multiple clouds with overlapping velocities from the quiescent galaxy disk (see Sect. 5.2).

However, several additional redshift-dependent biases ought to be considered for the detectability of absorption: first, contrary to the dust emission, which benefits from a negative  $K$ -correction, the AGN synchrotron emission intrinsically decreases with frequency, and becomes fainter at higher-redshift. Second, for a given observing frequency, the lines to be observed at higher-redshift correspond to higher  $J$ -level; these are increasingly difficult to excite in diffuse media, and may be more easily detected through absorption. Also, at higher-redshifts, higher-spatial-resolution is required to resolve the line emission and detect the underlying absorption signal.

### 5.2. Nature of the gas detected in intervening systems

Because of the low surface filling factor of the molecular gas and the compact size of the AGN continuum emission, the probability of detecting gas in distant galaxies through emission lines may be much higher than through line absorption. Indeed, CO and [C II] emission from strong metal absorbers or high- $z$  DLAs at  $z \sim 0.1$ –4 were recently detected with ALMA and NOEMA (Neeleman et al. 2016, 2019; Kaur et al. 2021, 2022). Typically, the H I column densities along the background quasar are of the order of  $10^{21} \text{ cm}^{-2}$ , and the galaxies have higher far-infrared

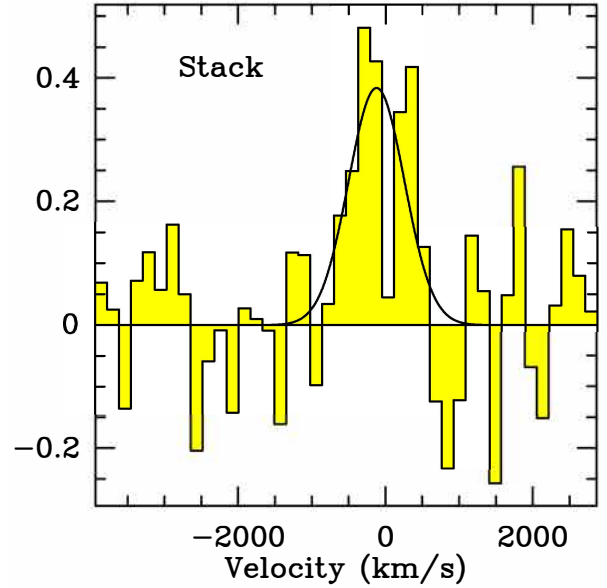


**Fig. 8.** Spectrum stacked from of all upper limits described in Table 4. The spectra were all aligned at the observed H I absorption velocity. The vertical scale is  $T_{\text{mb}}$  in mK. All continuum levels have been ignored.

luminosities than the Milky Way. Although the projected separation between a galaxy and a quasar can be relatively high, that is, 10–45 kpc for [C II] and as much as 100 kpc for CO, the velocities of emission and absorption signals are reasonably consistent. The inferred molecular gas masses are in the range of  $10^9$ – $10^{10.5} M_{\odot}$ . The intervening emission line detection in our sample have masses of  $M(\text{H}_2) = 7 \times 10^{11} M_{\odot}$  ( $z = 3.38715$ ) and  $1.5 \times 10^{10} M_{\odot}$  ( $z = 0.05151$ ; see Table 2). The CO emission detection rate is 2/14, which is  $\sim 14^{+19}_{-9}\%$ . Among 19 DLAs at  $z \sim 2$  with CO emission searches reported in the literature, the CO detection rate can be as high as  $56^{+38}_{-24}\%$  but only for high-metallicity ( $[\text{M}/\text{H}] > -0.3$ ) absorbers; otherwise it is merely  $\sim 11^{+26}_{-9}\%$  (Kaur et al. 2022). Notably, the  $z = 3.38715$  detection presented here has the lowest absorption metallicity  $[\text{M}/\text{H}] = -1.2$  (Kanekar et al. 2007) and the highest molecular mass among the DLAs investigated for CO emission to date. However, in relation to other DLAs at comparable redshifts, its metallicity is close to average (e.g., Rafelski et al. 2012).

#### 5.2.1. Individual sources

Now, we turn our attention to the molecular-absorption-line detections. Among the seven intervening systems in Table 5, three are associated with lensing galaxies. Toward PMN0134–0931, molecular absorption separated by  $\sim 200 \text{ km s}^{-1}$  is seen toward two sight lines separated by 5 kpc (Wiklind et al. 2018). The spatially unresolved 21 cm absorption spectrum shows smoother absorption coinciding with most of the molecular absorption (Kanekar & Briggs 2003). The H I and molecular absorption line column densities in Table 5 correspond to the deeper 21 cm absorption component with  $N(\text{CO})/N(\text{H I}) = 2.2 \times 10^{-4}$  ( $N(\text{H}_2)/N(\text{H I}) = 2.2$ ). The other absorption component exhibits different properties, with an abundance ratio that is lower by a factor of  $\sim 5$ . As previously noted, for PKS0201+113, the 21 cm, and H<sub>2</sub> absorption do not coincide, the peaks are separated by about  $\sim 25 \text{ km s}^{-1}$  (Srianand et al. 2012). Interestingly, the 21 cm absorption

**Table 5.** Comparison of 14 known HI 21 cm and molecular-absorption-line systems; the first 7 are associated and the remaining ones are intervening.

Target	$z_e$	$z_{21}^*$	$N(\text{HI})$ ( $\text{cm}^{-2}$ )	$FWHM$ ( $\text{km s}^{-1}$ )	$\int \tau dV$ ( $\text{km s}^{-1}$ )	$N(\text{H}_2)$ ( $\text{cm}^{-2}$ )	$FWHM$ ( $\text{km s}^{-1}$ )	$\int \tau dV$ ( $\text{km s}^{-1}$ )	Line	$z_{\text{mol}}$	Ref (H I)	Ref (Mol.)
(1)	(2)	(3)	(4)	(5)	(6)	(7)	(8)	(9)	(10)	(11)	(12)	(13)
J0439+0520	0.2076	–	<5e22	<200	<28.	2.0e21	126 (210)	5.4	CO(1–0)	0.2077	H1	C1
PKS 1200+045	1.2243	1.2111	4.6e21	100 (800)	2.52	1.5e20	87 (225)	3.1	CO(2–1)	1.21276	H2	C2
PKS 1245–197	1.275	1.2750	8.3e21	200 (1000)	4.54	3.6e20	113 (400)	7.2	CO(2–1)	1.26605	H2	C2
4C+12.50	0.1217	0.1217	6.6e21	250 (1800)	3.6	1.8e22	250 (600)	55.0	CO(3–2)	0.11806	H3	C3
B1504+377	0.674	0.67343	3.8e22	130 (175)	21.0	6.0e20	75 (100)	10.4	CO(2–1)	0.67343	H4	C4
B1740–517	0.4423	0.44129	5.0e21	5 (210)	2.7	1.5e20	37 (120)	4.8	CO(2–1)	0.44185	H5	H5
Abell 2390	0.2304	0.2310	2.5e+22	154 (1100)	13.7	8.0e21	122 (300)	28.2	CO(1–0)	0.2312	H6,H1	C1
PMN0134–0931	2.225	0.76344	9.0e20	107 (200)	4.93	2.0e21	53 (200)	70.3	CO(2–1)	0.76391	H7	C5
PKS 0201+113	3.639	3.38714	1.8e21	19 (125)	0.7	6.6e20	57 (400)	6.2	CO(4–3)	3.38715	H8	C2
B0218+357	0.944	0.68466	4.0e20	43 (75)	2.19	4.0e23	20 (30)	20.3	C <sup>18</sup> O(2–1)	0.68466	H9	C6, C7
G0248+430	1.313	0.05151	9.7e19	19 (90)	0.53	2.9e19	16 (30)	0.25	CO(1–0)	0.05151	H10	C8
PKS 1406–076	1.494	1.27464	2.5e20	11 (50)	0.51	1.0e23	77 (155)	2.4	HNC(2–1)	1.26949	H11	C2
PKS 1413+135	~0.3	0.24671	2.0e21	18 (180)	10.86	4.6e20	2 (5)	3.64	CO(1–0)	0.24671	H12	C9
PKS 1830–211	2.510	0.88489	1.8e21	180 (400)	10.1	4.0e22	40 (400)	30.	CO(4–3)	0.88582	H13	C10

**Notes.** Columns: (1, 2) favored name and systemic optical redshift; (3) redshift based on HI 21 cm absorption peak; (4, 6) total HI column density, adopting  $T_s = 1000$  K (100 K) for associated (intervening) targets, and integrated optical depth; (5) FWHM of the main absorption component; (7–9) molecular column density, FWHM and total integrated optical based on line in Col. (10); (11) redshift based on the peak of molecular line; (12) and (13) references for HI 21 cm and molecular absorption line. In Cols. (5) and (8), we also give the full velocity extent of the absorption in parentheses.

**References.** HI-ref – H1: Hogan (2014), H2: Aditya & Kanekar (2018), H3: Morganti et al. (2004), H4: Carilli et al. (1997), H5: Allison et al. (2019), H6: Hernández et al. (2008), H7: Carilli et al. (1993), H8: Kanekar et al. (2007), H9: Koopmans & de Bruyn (2005), H10: Gupta et al. (2018a), H11: Gupta et al. (2012), H12: Carilli et al. (1993), Combes et al. (2023), H13: Kanekar & Briggs (2003). CO-ref – C1: Rose et al. (2019a), C2: present work, C3: Dasyra & Combes (2012), C4: Wiklind & Combes (1996a), C5: Wiklind et al. (2018), C6: Wiklind & Combes (1995), C7: Combes & Wiklind (1995), C8: Combes et al. (2019), C9: Wiklind & Combes (1997), C10: Wiklind & Combes (1998). <sup>(\*)</sup>  $z_{21}$  is the redshift of peak HI 21 cm absorption depth, except for PKS 1200+045, where it is the center of the velocity range over which the absorption is detected.

and CO absorption components coincide rather well; that is, within  $5 \text{ km s}^{-1}$  (Fig. 3). These may be good candidates for constraining the variation of fundamental constants of physics using CO and 21 cm absorption, albeit with better quality spectra. The total integrated HI column density in Table 5 provides  $N(\text{CO})/N(\text{HI}) = 3.7 \times 10^{-5}$  ( $N(\text{H}_2)/N(\text{HI}) = 0.4$ ). This is a factor of two higher if only the HI in the main absorption component is considered. In general, the CO absorption does not extend over all 21 cm components because of the difference in radio continuum extent. The  $\text{H}_2$  column density based on Lyman and Werner band absorption lines is  $N(\text{H}_2) = 10^{14.6-16.0} \text{ cm}^{-2}$  (Srianand et al. 2012), which is about five orders of magnitude less than the value inferred from the CO absorption. This and the disparity between the  $\text{H}_2$  and 21 cm/CO absorption-line shifts suggest parsec-scale structure in the cloud.

The HI 21 cm absorption toward another lensed system, B0218+37, is much broader than the molecular line but the absorption peaks match well within  $10 \text{ km s}^{-1}$  (Wiklind & Combes 1995). The  $N(\text{CO})/N(\text{HI}) = 0.1$  ( $N(\text{H}_2)/N(\text{HI}) = 10^3$ ). The CO and  $^{13}\text{CO}$  lines are optically thick, and the column density is obtained through the C<sup>18</sup>O(2–1) line (Combes & Wiklind 1995). We must caution here that, given the different continuum sizes, the HI and  $\text{H}_2$  column densities are not averaged over the same apertures. As previously noted, the atomic and molecular absorption also match well for G0248+430, with  $N(\text{CO})/N(\text{HI}) = 2.9 \times 10^{-4}$  ( $N(\text{H}_2)/N(\text{HI}) = 2.9$ ), and 90% of the 21 cm optical depth is within the extent of molecular absorption. Toward PKS1413+135, the HI absorption is broad but the molecular absorption is extremely narrow, and  $N(\text{H}_2)/N(\text{HI}) = 0.2$ . PKS1830–211 is also a lensed system. In particular, it is known to

be rich in gas and dust, exhibiting more than sixty molecular transitions (Muller et al. 2014). Both the HI and CO absorptions are broad ( $\sim 400 \text{ km s}^{-1}$ ), and the overall  $N(\text{H}_2)/N(\text{HI}) = 22$ , which is among the highest levels known for this kind of object.

The case of PKS1406–076 is intriguing, with no overlap between the molecular and 21 cm line absorptions. The background radio source is a blazar that exhibits proper motion ( $0.3 \text{ mas yr}^{-1}$ ) and complex morphology at mas scales over 180 pc. The HI 21 cm absorption profile in the GMRT spectra shows three well-detached components and tentative variability over seven months (Gupta et al. 2012). The disparity between the 21 cm and mm molecular absorptions is attributable to the parsec-scale structure in the cloud; that is, the radio and mm sight lines trace different media. Unfortunately, the presence of HI 21 cm absorption corresponding to the HNC absorption is unknown. The GMRT observation to detect HI 21 cm absorption used a narrow (1 MHz) bandwidth to target the Mg II absorption and did not cover the 21 cm line frequency corresponding to the HNC absorption.

### 5.2.2. Summary

In summary, in the case of intervening absorbers, the HI absorption is broader and the narrower molecular absorption line is generally close to the HI absorption peak, albeit shifted by 10–20  $\text{km s}^{-1}$ . The exceptions are PKS1406–076 and the three lensed systems where the situation is complicated by multiple sightlines toward the lensed source. Nevertheless, the observed velocity structure of HI and the molecular absorption profiles imply sight lines piercing through layered molecular clouds; that is, molecular gas embedded in outer layers of predominantly HI gas.

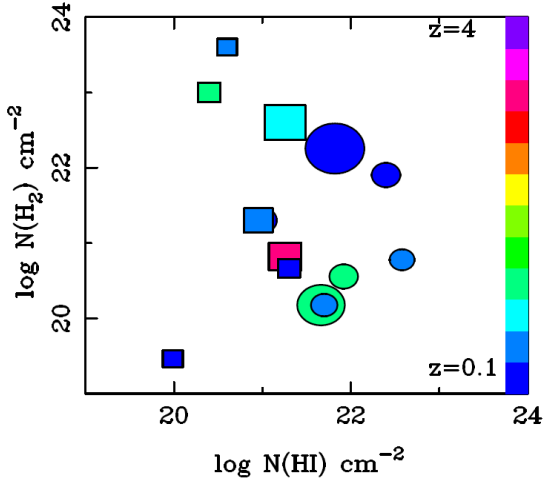


**Fig. 9.** Comparison between  $\text{H}_2$  and HI (21 cm) column densities for the known *molecular-absorption-line* systems at high-redshift.  $T_s = 1000$  K (100 K) is adopted for associated (intervening) systems shown as circles (squares). The color of the symbols represents the redshift, as indicated by the color bar on the right, and the size of the symbol traces the velocity extent of the absorption averaged over the HI and  $\text{H}_2$  components.

### 5.3. Nature of the gas detected in associated systems

Both associated targets, PKS 1200+045 and PKS 1245–19, detected in molecular absorption are GPS sources. In general, such sources are extremely compact ( $<1$  kpc) and are believed to represent the early stages of evolution of powerful radio galaxies (O’Dea & Saikia 2021). They are known to exhibit the highest HI 21 cm absorption detection rates ( $\sim 45\%$ ; Gupta et al. 2006). Indeed, five out of six CO emission-line detections from our sample are also GPS sources (Table 2). In all five cases, the CO emission line peak coincides with the systemic optical redshift within  $\sim 200$  km  $\text{s}^{-1}$  (Fig. 1). The CO emission line widths (FWHM) are 200–800 km  $\text{s}^{-1}$ , implying that these may have contributions from the gas clouds from (i) the host galaxy ISM through which the young radio source is expanding, and (ii) the circumnuclear disk, especially the regions close to the central AGN. The emission and absorption detected toward Abell 2390 is complex: the CO emission is extended and exhibits large-scale outflows and the HI 21 cm absorption has a narrow feature with broader components on either side or covering the entire velocity (Hernández et al. 2008; Rose et al. 2019a). Nevertheless, the HI absorption line peak in all but one source (i.e., PKS 1200+045) is also within the velocity range over which CO emission is detected. Therefore, to first-order, HI 21 cm absorption and CO mm emission lines are originating from the same regions.

In general, at cm wavelengths, the absorption is more likely to be detected in front of radio jets and lobes, whereas at mm wavelengths the gas in front of the flat spectrum “core” dominates the detected signal. In addition, molecular gas is embedded in ISM clouds with outer layers of higher atomic gas fraction. Both these factors, that is, geometrical effects – due to orientation and the frequency-dependent structure of the radio source – and varying molecular gas fraction within the cloud may lead to differences in the observed properties of the gas detected in atomic and molecular absorption lines.

In addition to the two associated CO absorbers reported here, associated molecular absorption lines have been detected in five other systems (see Table 5). In general, associated HI 21 cm absorption lines are known to exhibit a deep narrow component

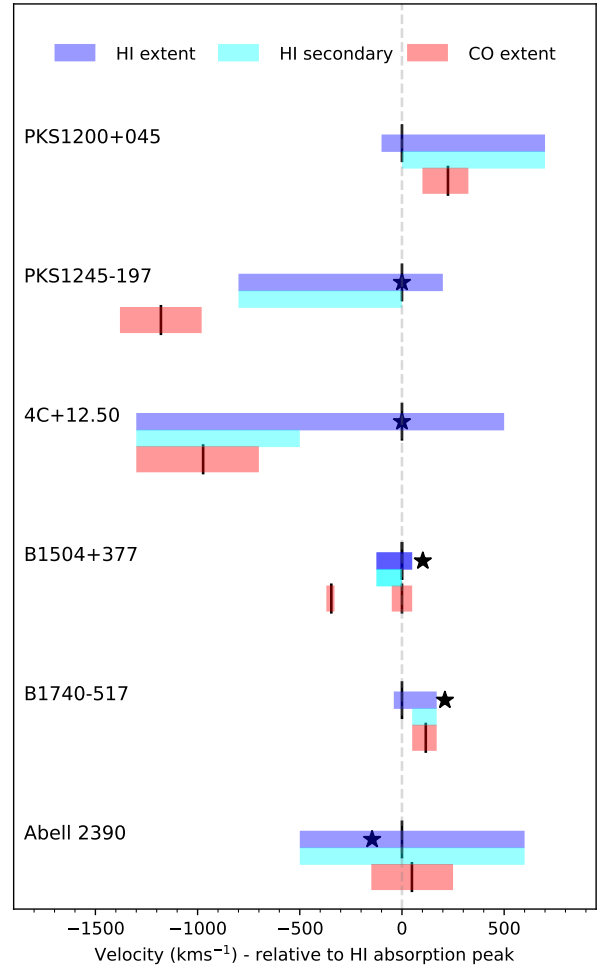


**Fig. 10.** Velocity offsets of HI 21 cm and CO absorption lines. The zero of the velocity scale corresponds to  $z_{21}$ . For HI, both the extent of the full and secondary absorption are shown. The vertical ticks mark the location of HI and CO absorption peaks, and the systemic velocity – except for PKS 1200+045 – based on optical emission lines is shown with a star  $\star$ .

and a broad shallow component. The former, when coincident with the systemic redshift, is believed to originate from the circumnuclear disk or torus. The latter, depending on whether it is blueshifted or redshifted with respect to the systemic redshift, is interpreted as outflowing gas due to jet–ISM interaction or infalling gas that may eventually fuel the AGN, respectively. In Fig. 10, we present the extent of the overall HI 21 cm absorption (in blue) and the associated secondary (i.e., broader/shallower) component (in cyan) for six AGNs<sup>2</sup>. In five of the six cases, the HI absorption peak, shown as a vertical blue line, matches the systemic redshift within  $\pm 200$  km  $\text{s}^{-1}$ . Interestingly, there is a tendency among the associated systems to present CO absorption (in red) coincident with the weaker 21 cm absorption component.

#### 5.3.1. Individual sources

For PKS 1200+045, the observed offset ( $\sim 2000$  km  $\text{s}^{-1}$ ) between the HI 21 cm and CO absorption lines with respect to molecular and optical/UV emission lines is particularly intriguing. The large velocity offset with respect to the CO emission lines and

<sup>2</sup> BCG J0439+0520 with no HI 21 cm absorption is excluded.

systemic redshift, and the widths of HI 21 cm ( $\sim 800 \text{ km s}^{-1}$ ) and CO ( $\sim 200 \text{ km s}^{-1}$ ) absorption lines suggest that the absorbing gas represents a distinct and scarce population of cold gas clouds in the host galaxy. The associated radio emission at 1.4 GHz with a projected linear size of 60 mas (500 pc at  $z_{\text{abs}}$ ) exhibits three components, one of which lies at one end and contains more than 90% of the total flux density (Liu et al. 2007). The nature of this one-sided morphology as a core–jet structure is confirmed by the higher-frequency milliarcsecond-scale images at 2.3, 4.3, and 8.7 GHz available from the Very Long Baseline Array (VLBA) calibrator catalog<sup>3</sup>. The one-sided core–jet morphology and orientation of the jet axis likely ensures that the sight lines to the radio source do not pass through the circumnuclear disk detected in CO emission. The absorbing gas may then correspond to quiescent clouds in the host galaxy ISM or gas interacting with the jet. The large velocity widths of HI 21 cm ( $\sim 800 \text{ km s}^{-1}$ ) and CO ( $\sim 200 \text{ km s}^{-1}$ ) absorption lines suggest that the latter is true, with the gas being detectable in absorption primarily due to the orientation of the radio source.

For PKS 1200+045 one possibility is that only the radio “core” is responsible for the absorption detected at cm and mm wavelengths. The HI absorption consists of two components separated by  $\sim 200 \text{ km s}^{-1}$  and CO absorption is coincident only with the secondary weaker component (Fig. 10). Assuming complete coverage of the radio core for the total integrated columns of the atomic and molecular gas, and  $T_s = 1000 \text{ K}$ , we estimate the CO-to-HI column-density ratio,  $N(\text{CO})/N(\text{HI}) = 3 \times 10^{-6}$ , which means  $N(\text{H}_2)/N(\text{HI}) = 3 \times 10^{-2}$ . Alternatively, it is also possible that only the CO and secondary HI absorption components are originating from the gas in front of the radio core. The molecular to HI column density ratio would then be a factor of two higher. The deeper HI absorption component would then correspond to the gas in front of the weaker radio components associated with the jet and the lobe. The projected distance of this gas component would be at least a few hundred parsecs from the core, which would explain the absence of CO absorption at the corresponding velocities.

The second possibility for PKS 1200+045 is similar to the scenario observed for 4C+12.50: a CSS source hosted in a gas-rich Seyfert galaxy. At 1.4 GHz, 4C+12.50 exhibits a distorted radio morphology with an overall extent of 150 mas ( $\sim 325 \text{ pc}$ ). The mas-scale spectroscopy reveals the deep, narrow HI 21 cm absorption component that is detected toward the fainter northern lobe rather than the core or the brighter southern hotspot (Morganti et al. 2004). The weaker HI absorption component coincides with the CO absorption. The CO-to-HI column density ratio is  $6 \times 10^{-4}$  ( $N(\text{H}_2)/N(\text{HI}) = 6$ ) for  $N(\text{HI}) = 3 \times 10^{21} \text{ cm}^{-2}$  based on the Na I or HI 21 cm absorption ( $T_s = 1000 \text{ K}$ ) associated with the absorption component coincident with the molecular absorption. This is about 200 times higher than the ratio observed for PKS 1200+045 and is likely due to the fact that 4C+12.50 (i) is hosted in a gas-rich Seyfert galaxy, and (ii), being a radio galaxy, PKS 1200+045 is oriented such that the sight line to the radio core passes through the circumnuclear disk.

In contrast to PKS 1200+045, the CO absorption associated with PKS 1245–19 is offset with respect to the 21 cm absorption by  $-1180 \text{ km s}^{-1}$  but is within the range over which CO emission is detected (Fig. 7). The 21 cm absorption coincides well with the CO emission (Fig. 7). At 2.3 and 8.6 GHz, the radio source exhibits two prominent, steep spectrum ( $\alpha < -0.5$ ) components of similar strength, separated by  $\sim 25 \text{ mas}$  (Sokolovsky et al.

2011). The radio core is not detected in these low-frequency images but may be responsible for the CO absorption. The sight lines at cm wavelengths, especially those toward the counter jet and lobe, pass through the circumnuclear disk as well as the host galaxy ISM. The nondetection of HI 21 cm absorption – adopting  $T_s = 1000 \text{ K}$  and a line  $FWHM = 200 \text{ km s}^{-1}$  based on the detected CO absorption – corresponds to a CO-to-HI column density ratio of  $> 7 \times 10^{-5}$  ( $N(\text{H}_2)/N(\text{HI}) > 0.7$ ). This is significantly higher and lower than the ratios observed for PKS 1200+045 and 4C+12.50, respectively. Overall, both the 21 cm and CO absorption lines seem to be tracing the galaxy-wide cold gas from the ISM and the circumnuclear disk detected in CO emission. The disparity between HI and CO absorption lines is most likely due to the differences in the sight lines at cm and mm wavelengths.

Molecular absorption lines have also been detected toward B1504+377, which is hosted by a disk galaxy. The associated radio emission at cm wavelengths consists of a dominant ‘core’ component, with some diffuse emission at a distance of 55 mas (390 pc at  $z = 0.674$ ). There is coincidence between the broader HI and CO absorption ( $FWHM \sim 75 \text{ km s}^{-1}$ ) components at  $z = 0.67343$ , both of which are coincident with the systemic velocity (Wiklind & Combes 1996a; Carilli et al. 1997). However, no HI absorption is detected in the narrow ( $FWHM \sim 15 \text{ km s}^{-1}$ ) molecular absorption component at  $z = 0.67150$  (see Fig. 10). For the broader component, the CO-to-HI column-density ratio is  $2 \times 10^{-6}$  ( $N(\text{H}_2)/N(\text{HI}) > 0.02$ ). The orientation and the morphology of the radio source suggest that it is tracing the gas through the circumnuclear disk as intercepted by the core. The nondetection of HI 21 cm absorption in the narrow CO absorption component corresponds to a column density ratio of  $> 3 \times 10^{-5}$  ( $N(\text{H}_2)/N(\text{HI}) > 0.3$ ), which is comparable to other similar systems discussed here but is at least a factor of ten higher than the broader component. Based on the large shift ( $-450 \text{ km s}^{-1}$ ) but narrow width ( $15 \text{ km s}^{-1}$ ), it likely represents a cloud in the inner circumnuclear disk. The HI 21 cm absorption nondetection is due to the relatively high CO-to-HI abundance ratio.

Another molecular absorber is B1740–517, which is a GPS source associated with a radio galaxy (Sy). At 2.3 GHz, radio emission is resolved into two components separated by  $\sim 50 \text{ mas}$  ( $\sim 300 \text{ pc}$  at  $z = 0.442$ ) and the CO(2–1) absorption coincides with a weaker HI absorption component (Allison et al. 2019). No CO absorption is detected at the narrow, deep 21 cm absorption peak, which is blueshifted with respect to the CO absorption and the systemic redshift by  $\sim 130 \text{ km s}^{-1}$ . It is unclear whether the two radio components are core–jet or two lobes. The CO-to-HI column density ratio for the absorption component with HI and CO absorption,  $2 \times 10^{-5}$  ( $N(\text{H}_2)/N(\text{HI}) = 0.2$ ), is comparable to those of other associated systems. It may represent gas closer to the central AGN, whereas the narrow component represents distant gas toward the jet and the lobe.

### 5.3.2. Summary

Overall, CO absorption is generally detected in broader and weaker 21 cm absorption components with typical CO-to-HI abundance ratios of  $10^{-6}$ – $10^{-5}$  ( $N(\text{H}_2)/N(\text{HI}) = 0.01$ – $0.1$ ). Except for B1504+377, the CO absorption never coincides with the deep, strong 21 cm absorption component. This suggests that absorbing gas has two different phases: one phase near galaxy centers with a larger CO-to-HI abundance ratio, and another with lower CO abundance that shows only HI and might correspond to the gas in outer regions of galaxies. These two phases are

<sup>3</sup> <https://obs.vlba.nrao.edu/cst/>

well known through emission-line observations of nearby galaxies (e.g., Bigiel & Blitz 2012). The detection rate of molecular absorption from our survey is 2/16, which equates to  $13_{-8}^{+16}\%$ . As mentioned above, the detection of molecular absorption is not expected in all associated systems with 21 cm absorption because of the smaller filling factor of the molecular component, and the much smaller continuum sizes at mm frequency.

## 6. Conclusions

We searched for molecular emission and absorption in 30 HI 21 cm absorbers at  $0.1 < z < 4$ . Of these, 16 are associated with the AGN and the remaining 14 are from intervening galaxies. We report the detection of CO emission in 8 systems, of which 5 are new. The derived molecular masses, assuming standard conversion ratios, range from  $10^9$  to  $7 \times 10^{11} M_{\odot}$ . The majority of these correspond to associated systems belonging to young radio AGN, that is, intrinsically compact radio sources with a peaked radio spectrum. Four of them are at low redshift ( $z < 0.25$ ). Intervening galaxies that show CO emission are rarer ( $2/14 \approx 14_{-9}^{+19}\%$ ). The two detections reported here from our sample have masses of  $M(\text{H}_2) = 7 \times 10^{11} M_{\odot}$  (PKS 0201+113;  $z = 3.38715$ ) and  $1.5 \times 10^{10} M_{\odot}$  (Q0248+430;  $z = 0.05151$ ). Notably, the  $z = 3.38715$  detection presented here has the lowest absorption metallicity ( $[\text{M}/\text{H}] = -1.2$ ) and the highest molecular mass among the DLAs investigated for CO emission to date (Kaur et al. 2022). We note that the average metallicity of DLAs at such high-redshifts is  $[\text{M}/\text{H}] \sim -1.5$  (Rafelski et al. 2012). We also stacked together the spectra from 21 undetected sources (10 associated and 11 intervening) and find a hint of emission, that is, at a flux level of about an order of magnitude lower than the individual detections. It is not possible to draw conclusions on the corresponding masses because of the varied distances.

Millimeter molecular absorptions are still very rare at moderate and high-redshift: only ten systems have been found (Combes 2008; Dasyra & Combes 2012; Wiklind et al. 2018; Allison et al. 2019; Combes et al. 2019; Rose et al. 2019a): five are associated absorbing systems, and the remaining five are intervening systems, of which three are gravitational lenses. Here, we report four systems showing absorption line detections, two associated and two intervening. The two associated systems, PKS 1200+045 ( $z = 1.2111$ ) and PKS 1245–19 ( $z = 1.2750$ ), were detected in high-spatial-resolution NOEMA follow-up observations of our IRAM 30 m detection of CO emission, and demonstrate the complexity faced in detecting absorption in the presence of emission. Alternatively, it is possible to detect absorption in the high-density tracers, such as  $\text{HCO}^+$ , HCN, or HNC, which are not detectable in emission. This is indeed the case for the intervening system toward PKS1406–076 ( $z = 1.27464$ ) reported here.

The other two intervening detections are toward PKS0201+113 ( $z = 3.38714$ ) and Q0248+430 (0.05151) (Combes et al. 2019). For PKS0201+113, the 21 cm, and  $\text{H}_2$  (ultraviolet) absorption components do not coincide; the peaks are separated by about  $\sim 25 \text{ km s}^{-1}$  (Srianand et al. 2012). Interestingly, the 21 cm absorption and CO absorption components coincide rather well (i.e., within  $5 \text{ km s}^{-1}$ ; Fig. 3), and the latter could be good candidates with which to constrain the variations of fundamental constants of physics. The disparity between  $\text{H}_2$  and 21 cm/CO absorption line shifts suggests parsec-scale structure in the cloud. The case of PKS1406–076 is even more intriguing, with no overlap between the molecular and 21 cm line absorptions. The disparity between the 21 cm and mm molecular absorptions is attributable to complex radio

morphology; that is, radio and mm sight lines tracing different media.

We compare the atomic and molecular column densities of 14 known high-redshift ( $z > 0.1$ ) molecular absorption line systems. Among associated systems, CO absorption is generally detected in the broader and weaker 21 cm absorption component, with a typical CO-to-HI abundance ratio of  $10^{-6}$ – $10^{-5}$  ( $N(\text{H}_2)/N(\text{HI}) = 0.01$ – $0.1$ ). The CO absorption very rarely coincides with the deep and narrow 21 cm absorption component. This suggests that absorbing gas has two different phases: one phase near to galaxy centers with a larger CO-to-HI abundance ratio, and another with lower CO abundance that shows only HI and might correspond to the gas in outer regions of galaxies. These two phases are well known through emission line observations of nearby galaxies (e.g., Bigiel & Blitz 2012).

In the case of intervening absorbers, the HI absorption is broader and the narrower molecular absorption line is generally close to the HI absorption peak, although shifted by  $10$ – $20 \text{ km s}^{-1}$ . The exceptions are PKS1406–076 and the three lensed systems where the situation is complicated by multiple sightlines toward the lensed source. Nevertheless, the observed velocity structure of HI and molecular absorption profiles imply sight lines piercing through layered molecular clouds; that is, molecular gas embedded in outer layers of predominantly HI gas.

With the advent of large surveys at cm wavelengths, the number of HI 21 cm absorbers is expected to steeply increase. However, currently, HI 21 cm line spectroscopy at  $z > 0.5$  can be performed only at spatial resolutions of  $>5''$ , which may be insufficient to reveal the origin of the absorbing gas. The work presented here demonstrates that this limitation can be overcome through the combination of mm emission and absorption spectroscopy, and helps to elucidate the role played by cold gas in the evolution of normal and active galaxies.

*Acknowledgements.* We sincerely thank the referee for very useful and constructive comments, and a thorough reading of the manuscript. This work is based on observations carried out with the IRAM-30 m telescope, and the NOEMA Interferometer. IRAM is supported by INSU/CNRS (France), MPG (Germany), and IGN (Spain). We acknowledge the help of the IRAM teams for the observations and thank Vinodiran Arumugam for his support with the data reduction. The data were processed using the Gildas package. This project has benefited from support from the Programme National Cosmologie et Galaxies. We made use of the NASA/IPAC Extragalactic Database (NED), and of the HyperLeda database (<http://leda.univ-lyon1.fr>).

## References

- Aditya, J. N. H. S. 2019, *MNRAS*, **482**, 5597
- Aditya, J. N. H. S., & Kanekar, N. 2018, *MNRAS*, **473**, 59
- Allison, J. R., Sadler, E. M., Moss, V. A., et al. 2015, *MNRAS*, **453**, 1249
- Allison, J. R., Mahony, E. K., Moss, V. A., et al. 2019, *MNRAS*, **482**, 2934
- Audibert, A., Dasyra, K. M., Papachristou, M., et al. 2022, *A&A*, **668**, A67
- Bagdonaite, J., Jansen, P., Henkel, C., et al. 2013, *Science*, **339**, 46
- Bell, M. B., & Seaquist, E. R. 1980, *ApJ*, **238**, 818
- Berg, T. A. M., Ellison, S. L., Prochaska, J. X., Venn, K. A., & Dessauges-Zavadsky, M. 2015, *MNRAS*, **452**, 4326
- Bigiel, F., & Blitz, L. 2012, *ApJ*, **756**, 183
- Bolatto, A. D., Wolfire, M., & Leroy, A. K. 2013, *ARA&A*, **51**, 207
- Bottinelli, S., Hughes, A. M., van Dishoeck, E. F., et al. 2009, *ApJ*, **690**, L130
- Carilli, C. L., Rupen, M. P., & Yanny, B. 1993, *ApJ*, **412**, L59
- Carilli, C. L., Menten, K. M., Reid, M. J., & Rupen, M. P. 1997, *ApJ*, **474**, L89
- Carswell, R. F., Jorgenson, R. A., Wolfe, A. M., & Murphy, M. T. 2011, *MNRAS*, **411**, 2319
- Chowdhury, A., Kanekar, N., & Chengalur, J. N. 2020, *ApJ*, **900**, L30
- Combes, F. 2008, *Ap&SS*, **313**, 321
- Combes, F., & Wiklind, T. 1995, *A&A*, **303**, L61
- Combes, F., Maoli, R., & Omont, A. 1999, *A&A*, **345**, 369
- Combes, F., Gupta, N., Jozsa, G. I. G., & Momjian, E. 2019, *A&A*, **623**, A133

- Combes, F., Gupta, N., Muller, S., et al. 2023, *A&A*, 671, A43
- Curran, S. J., Tzanavaris, P., Murphy, M. T., Webb, J. K., & Pihlström, Y. M. 2007, *MNRAS*, 381, L6
- Dannerbauer, H., Daddi, E., Riechers, D. A., et al. 2009, *ApJ*, 698, L178
- Dasyra, K. M., & Combes, F. 2012, *A&A*, 541, L7
- Dasyra, K. M., Combes, F., Novak, G. S., et al. 2014, *A&A*, 565, A46
- Decarli, R., Aravena, M., Boogaard, L., et al. 2020, *ApJ*, 902, 110
- Downes, D., Solomon, P. M., & Radford, S. J. E. 1993, *ApJ*, 414, L13
- Dutta, R., Srianand, R., Gupta, N., et al. 2017, *MNRAS*, 465, 4249
- Dutta, R., Srianand, R., & Gupta, N. 2019, *MNRAS*, 489, 1099
- Ellison, S. L., Pettini, M., Steidel, C. C., & Shapley, A. E. 2001, *ApJ*, 549, 770
- Ellison, S. L., Yan, L., Hook, I. M., et al. 2002, *A&A*, 383, 91
- Eracleous, M., & Halpern, J. P. 2004, *ApJS*, 150, 181
- Gupta, N., Salter, C. J., Saikia, D. J., Ghosh, T., & Jeyakumar, S. 2006, *MNRAS*, 373, 972
- Gupta, N., Srianand, R., Petitjean, P., et al. 2007, *ApJ*, 654, L111
- Gupta, N., Srianand, R., Baan, W., et al. 2016, *MeerKAT Science: On the Pathway to the SKA*, 14
- Gupta, N., Momjian, E., Srianand, R., et al. 2018a, *ApJ*, 860, L22
- Gupta, N., Srianand, R., Farnes, J. S., et al. 2018b, *MNRAS*, 476, 2432
- Gupta, N., Srianand, R., Petitjean, P., Noterdaeme, P., & Saikia, D. J. 2009, *MNRAS*, 398, 201
- Gupta, N., Srianand, R., Petitjean, P., et al. 2012, *A&A*, 544, A21
- Gupta, N., Srianand, R., Shukla, G., et al. 2021, *ApJS*, 255, 28
- Hamanowicz, A., Zwaan, M. A., Péroux, C., et al. 2023, *MNRAS*, 519, 34
- Henkel, C., Jethava, N., Kraus, A., et al. 2005, *A&A*, 440, 893
- Henkel, C., Menten, K. M., Murphy, M. T., et al. 2009, *A&A*, 500, 725
- Hernández, H., Ghosh, T., Salter, C. J., & Momjian, E. 2008, in *The evolution of galaxies through the neutral hydrogen window*, eds. R. Minchin, & E. Momjian, *AIP Conf. Ser.*, 1035, 214
- Hogan, M. T. 2014, PhD Thesis, Durham University, UK
- Holt, J., Tadhunter, C. N., & Morganti, R. 2003, *MNRAS*, 342, 227
- Hwang, C.-Y., & Chiou, S.-H. 2004, *ApJ*, 600, 52
- Kanekar, N. 2011, *ApJ*, 728, L12
- Kanekar, N., & Briggs, F. H. 2003, *A&A*, 412, L29
- Kanekar, N., & Chengalur, J. N. 2001, *A&A*, 369, 42
- Kanekar, N., Ghosh, T., & Chengalur, J. N. 2001, *A&A*, 373, 394
- Kanekar, N., Chengalur, J. N., & Lane, W. M. 2007, *MNRAS*, 375, 1528
- Kanekar, N., Langston, G. I., Stocke, J. T., Carilli, C. L., & Menten, K. M. 2012, *ApJ*, 746, L16
- Kaur, B., Kanekar, N., Rafelski, M., et al. 2021, *ApJ*, 921, 68
- Kaur, B., Kanekar, N., Rafelski, M., et al. 2022, *ApJ*, 933, L42
- Klitsch, A., Péroux, C., Zwaan, M. A., et al. 2019, *MNRAS*, 490, 1220
- Kollatschny, W., Dietrich, M., Borgeest, U., & Schramm, K. J. 1991, *A&A*, 249, 57
- Koopmans, L. V. E., & de Bruyn, A. G. 2005, *MNRAS*, 360, L6
- Kuehr, H. 1977, *A&AS*, 29, 139
- Labiano, A., Barthel, P. D., O’Dea, C. P., et al. 2007, *A&A*, 463, 97
- Lenkić, L., Bolatto, A. D., Förster Schreiber, N. M., et al. 2020, *AJ*, 159, 190
- Liszt, H., & Lucas, R. 2001, *A&A*, 370, 576
- Liu, X., Cui, L., Luo, W. F., Shi, W. Z., & Song, H. G. 2007, *A&A*, 470, 97
- Madau, P., & Dickinson, M. 2014, *ARA&A*, 52, 415
- Maloney, P. R., Hollenbach, D. J., & Tielens, A. G. G. M. 1996, *ApJ*, 466, 561
- Menten, K. M., Güsten, R., Leurini, S., et al. 2008, *A&A*, 492, 725
- Morganti, R., Oosterloo, T. A., Tadhunter, C. N., et al. 2004, *A&A*, 424, 119
- Muller, S., Beelen, A., Black, J. H., et al. 2013, *A&A*, 551, A109
- Muller, S., Combes, F., Guélin, M., et al. 2014, *A&A*, 566, A112
- Muller, S., Müller, H. S. P., Black, J. H., et al. 2016, *A&A*, 595, A128
- Muller, S., Ubachs, W., Menten, K. M., Henkel, C., & Kanekar, N. 2021, *A&A*, 652, A5
- Murphy, M. T., Molero, P., Leite, A. C. O., et al. 2022, *A&A*, 658, A123
- Neeleman, M., Prochaska, J. X., Zwaan, M. A., et al. 2016, *ApJ*, 820, L39
- Neeleman, M., Kanekar, N., Prochaska, J. X., Rafelski, M. A., & Carilli, C. L. 2019, *ApJ*, 870, L19
- Noterdaeme, P., Petitjean, P., & Srianand, R. 2015, *A&A*, 578, L5
- Noterdaeme, P., Balashev, S., Cuellar, R., et al. 2023, *A&A*, 673, A89
- Obreschkow, D., & Rawlings, S. 2009a, *ApJ*, 696, L129
- Obreschkow, D., & Rawlings, S. 2009b, *MNRAS*, 394, 1857
- Ocaña Flaquer, B., Leon, S., Combes, F., & Lim, J. 2010, *A&A*, 518, A9
- O’Dea, C. P., & Saikia, D. J. 2021, *A&ARv*, 29, 3
- Peck, A. B., Taylor, G. B., & Conway, J. E. 1999, *ApJ*, 521, 103
- Petitjean, P., Srianand, R., & Ledoux, C. 2000, *A&A*, 364, L26
- Quider, A. M., Nestor, D. B., Turnshek, D. A., et al. 2011, *AJ*, 141, 137
- Rachford, B. L., Snow, T. P., Destree, J. D., et al. 2009, *ApJS*, 180, 125
- Rafelski, M., Wolfe, A. M., Prochaska, J. X., Neeleman, M., & Mendez, A. J. 2012, *ApJ*, 755, 89
- Readhead, A. C. S., Ravi, V., Lioudakis, I., et al. 2021, *ApJ*, 907, 61
- Riechers, D. A., Boogaard, L. A., Decarli, R., et al. 2020, *ApJ*, 896, L21
- Rose, T., Edge, A. C., Combes, F., et al. 2019a, *MNRAS*, 489, 349
- Rose, T., Edge, A. C., Combes, F., et al. 2019b, *MNRAS*, 485, 229
- Rose, T., Edge, A. C., Combes, F., et al. 2020, *MNRAS*, 496, 364
- Scoville, N. Z., Evans, A. S., Thompson, R., et al. 2000, *AJ*, 119, 991
- Shen, Y., Richards, G. T., Strauss, M. A., et al. 2011, *ApJS*, 194, 45
- Snellen, I. A. G., Lehnert, M. D., Bremer, M. N., & Schilizzi, R. T. 2003, *MNRAS*, 342, 889
- Sokolovsky, K. V., Kovalev, Y. Y., Pushkarev, A. B., Mimica, P., & Peruchó, M. 2011, *A&A*, 535, A24
- Solomon, P. M., & Vanden Bout, P. A. 2005, *ARA&A*, 43, 677
- Solomon, P. M., Radford, S. J. E., & Downes, D. 1992, *Nature*, 356, 318
- Srianand, R., Noterdaeme, P., Ledoux, C., & Petitjean, P. 2008, *A&A*, 482, L39
- Srianand, R., Gupta, N., Petitjean, P., et al. 2012, *MNRAS*, 421, 651
- Srianand, R., Gupta, N., Rahmani, H., et al. 2013, *MNRAS*, 428, 2198
- Stickel, M., & Kuhr, H. 1993, *A&AS*, 101, 521
- Tacconi, L. J., Genzel, R., Saintonge, A., et al. 2018, *ApJ*, 853, 179
- Tremblay, G. R., Oonk, J. B. R., Combes, F., et al. 2016, *Nature*, 534, 218
- Uzan, J.-P. 2011, *Liv. Rev. Relat.*, 14, 2
- Vermeulen, R. C., Pihlström, Y. M., Tschager, W., et al. 2003, *A&A*, 404, 861
- Weiß, A., Downes, D., Neri, R., et al. 2007, *A&A*, 467, 955
- White, R. L., Kinney, A. L., & Becker, R. H. 1993, *ApJ*, 407, 456
- Wiklind, T., & Combes, F. 1994, *A&A*, 286, L9
- Wiklind, T., & Combes, F. 1995, *A&A*, 299, 382
- Wiklind, T., & Combes, F. 1996a, *A&A*, 315, 86
- Wiklind, T., & Combes, F. 1996b, *Nature*, 379, 139
- Wiklind, T., & Combes, F. 1997, *A&A*, 328, 48
- Wiklind, T., & Combes, F. 1998, *ApJ*, 500, 129
- Wiklind, T., Combes, F., & Kanekar, N. 2018, *ApJ*, 864, 73
- Wolfe, A. M., Turnshek, D. A., Smith, H. E., & Cohen, R. D. 1986, *ApJS*, 61, 249